

# Low-temperature hydrogen production from water and methanol using Pt/ $\alpha$ -MoC catalysts

Lili Lin<sup>1\*</sup>, Wu Zhou<sup>2,3\*</sup>, Rui Gao<sup>4,5\*</sup>, Siyu Yao<sup>1</sup>, Xiao Zhang<sup>6</sup>, Wenqian Xu<sup>7</sup>, Shijian Zheng<sup>8</sup>, Zheng Jiang<sup>9</sup>, Qiaolin Yu<sup>1</sup>, Yong-Wang Li<sup>4,5</sup>, Chuan Shi<sup>6</sup>, Xiao-Dong Wen<sup>4,5</sup> & Ding Ma<sup>1</sup>

**Polymer electrolyte membrane fuel cells (PEMFCs) running on hydrogen are attractive alternative power supplies for a range of applications<sup>1–3</sup>, with *in situ* release of the required hydrogen from a stable liquid offering one way of ensuring its safe storage and transportation<sup>4,5</sup> before use. The use of methanol is particularly interesting in this regard, because it is inexpensive and can reform itself with water to release hydrogen with a high gravimetric density of 18.8 per cent by weight. But traditional reforming of methanol steam operates at relatively high temperatures (200–350 degrees Celsius)<sup>6–8</sup>, so the focus for vehicle and portable PEMFC applications<sup>9</sup> has been on aqueous-phase reforming of methanol (APRM). This method requires less energy, and the simpler and more compact device design allows direct integration into PEMFC stacks<sup>10,11</sup>. There remains, however, the need for an efficient APRM catalyst. Here we report that platinum (Pt) atomically dispersed on  $\alpha$ -molybdenum carbide ( $\alpha$ -MoC) enables low-temperature (150–190 degrees Celsius), base-free hydrogen production through APRM, with an average turnover frequency reaching 18,046 moles of hydrogen per mole of platinum per hour. We attribute this exceptional hydrogen production—which far exceeds that of previously reported low-temperature APRM catalysts—to the outstanding ability of  $\alpha$ -MoC to induce water dissociation, and to the fact that platinum and  $\alpha$ -MoC act in synergy to activate methanol and then to reform it.**

Pioneering work from 15 years ago<sup>12,13</sup> showed that hydrogen can be generated by aqueous-phase reforming of biomass-derived carbohydrates, including methanol, on platinum/aluminium oxide catalysts. More recently, use of a single nuclear [RuHCl(CO)(HN(C<sub>2</sub>H<sub>4</sub>PiPr<sub>2</sub>)<sub>2</sub>)] homogenous catalyst<sup>14</sup> enabled hydrogen to form at an unprecedented rate of 4,700 mol hydrogen per mol ruthenium per hour in the presence of concentrated potassium hydroxide solution and neat methanol at around 368 K. One main advantage of such homogeneous catalysts<sup>14,15</sup>, and of metalloenzymes<sup>16</sup>, is that each metal site in the catalyst contributes directly to the reaction—a fact that has stimulated much work on dispersing catalytically active noble metals as isolated metal atoms on support materials, to improve the efficiency of heterogeneous catalysts while minimizing the amount of noble metal used<sup>17–19</sup>. However, in order to achieve a high rate of hydrogen production from the reaction of methanol and water at low temperatures, both the water and the methanol must be activated effectively, and this may be difficult to achieve with a catalyst that contains only isolated noble-metal sites.

We reasoned that bifunctional structures might be important, with a suitable material not only acting as a support for confined metal atoms, but also modulating their electronic structure (given that the ligand of the high-performing homogeneous APRM catalyst mentioned above has been proposed<sup>14</sup> to have a crucial role as a hydrogen acceptor and in

promoting the cleavage of carbon–hydrogen bonds at the metal centre). Because the electronic structure of metal catalysts can be tuned by their supports or promoters<sup>20,21</sup>, and because electron-deficient platinum nanoparticles have been proposed to be responsible for the high activity of the low-temperature water–gas shift reaction<sup>18,20</sup>, careful choice of the support material for platinum should in principle make it possible to obtain bifunctional constructs with atomically dispersed noble-metal sites that catalyse low-temperature APRM.

In investigating possible support materials, we discovered that  $\alpha$ -MoC (face-centred-cubic (fcc) structure; hexoctahedral ( $Fm\bar{3}m$ ) space group) exhibits stronger interactions with platinum than do common oxide supports or  $\beta$ -Mo<sub>2</sub>C (hexagonal close-packed; tetragonal ( $P63/mmc$ ) space group). Driven by this strong interaction, platinum forms an atomic dispersion (termed Pt<sub>1</sub>) over  $\alpha$ -MoC during a high-temperature activation process, generating an exceptionally high density of electron-deficient surface Pt<sub>1</sub> sites for the adsorption/activation of methanol. Meanwhile the substrate,  $\alpha$ -MoC, shows high water-dissociation activity, producing abundant surface hydroxyls that accelerate the reforming of reaction intermediates at the interface between platinum and  $\alpha$ -MoC. These two effects combine to confer the platinum/ $\alpha$ -MoC catalyst with unprecedented catalytic efficiency (the average turnover frequency, ATOF, is 18,046 h<sup>−1</sup>) and good stability in the base-free APRM process at 150–190 °C.

We prepared platinum-modified molybdenum carbide catalysts (around 2 wt% platinum, unless otherwise specified) by using temperature-programmed carburization (TPC) of a mixture of methane and hydrogen with different precursors (see Methods). The catalysts are denoted hereafter as x%Pt/ $\alpha$ -MoC, 2%Pt/MoC-2, 2%Pt/MoC-3 and 2%Pt/ $\beta$ -Mo<sub>2</sub>C. X-ray diffraction (XRD; Fig. 1a) showed that the crystal phase of molybdenum carbide in Pt/ $\alpha$ -MoC is pure  $\alpha$ -MoC, while the crystal phases of 2%Pt/MoC-2 and 2%Pt/MoC-3 contain a mixture of  $\alpha$ -MoC and  $\beta$ -Mo<sub>2</sub>C, with 70.1% and 44.7% of  $\alpha$ -MoC, respectively (Extended Data Fig. 1a).

For platinum supported on pure  $\beta$ -Mo<sub>2</sub>C (2%Pt/ $\beta$ -Mo<sub>2</sub>C), we detected a small ATOF at 190 °C (168 mol H<sub>2</sub> per mol Pt per hour), similar to the values seen for oxide-supported platinum catalysts (Al<sub>2</sub>O<sub>3</sub> and TiO<sub>2</sub>; entries 8 and 9 in Table 1). When we mixed a fraction of  $\alpha$ -MoC with  $\beta$ -Mo<sub>2</sub>C to host the platinum, we observed a marked increase in activity (Fig. 1b and entries 5–7 in Table 1). For 2%Pt/ $\alpha$ -MoC (with pure  $\alpha$ -MoC), the average rate of hydrogen generation reaches 129.6 μmol hydrogen per gram catalyst per second (ATOF = 4,130 h<sup>−1</sup>) at 190 °C—a value that is more than an order of magnitude higher than that seen with the platinum/oxide catalysts. When we decreased the platinum loading the Pt/ $\alpha$ -MoC catalysts to 0.2%, the intrinsic activity increased still more (ATOF = 18,046 h<sup>−1</sup>). Notably, no base was involved in the whole process, making it both

<sup>1</sup>College of Chemistry and Molecular Engineering, Peking University, Beijing 100871, China. <sup>2</sup>School of Physical Sciences, CAS Key Laboratory of Vacuum Physics, University of Chinese Academy of Sciences, Beijing 100049, China. <sup>3</sup>Materials Science and Technology Division, Oak Ridge National Laboratory, Oak Ridge, Tennessee 37831, USA. <sup>4</sup>State Key Laboratory of Coal Conversion, Institute of Coal Chemistry, Chinese Academy of Sciences, PO Box 165, Taiyuan, Shanxi 030001, China. <sup>5</sup>Synfuels China Co. Ltd, Beijing 100195, China. <sup>6</sup>Key Laboratory of Industrial Ecology and Environmental Engineering (MOE), Dalian University of Technology, Dalian 116024, China. <sup>7</sup>X-ray Science Division, Advanced Photon Source, Argonne National Laboratory, Argonne, Illinois 60439, USA. <sup>8</sup>Shenyang National Laboratory for Materials Science, Institute of Metal Research, Chinese Academy of Sciences, Shenyang 110016, China. <sup>9</sup>Shanghai Institute of Applied Physics, Chinese Academy of Sciences, Shanghai, 201204, China.

\*These authors contributed equally to this work.

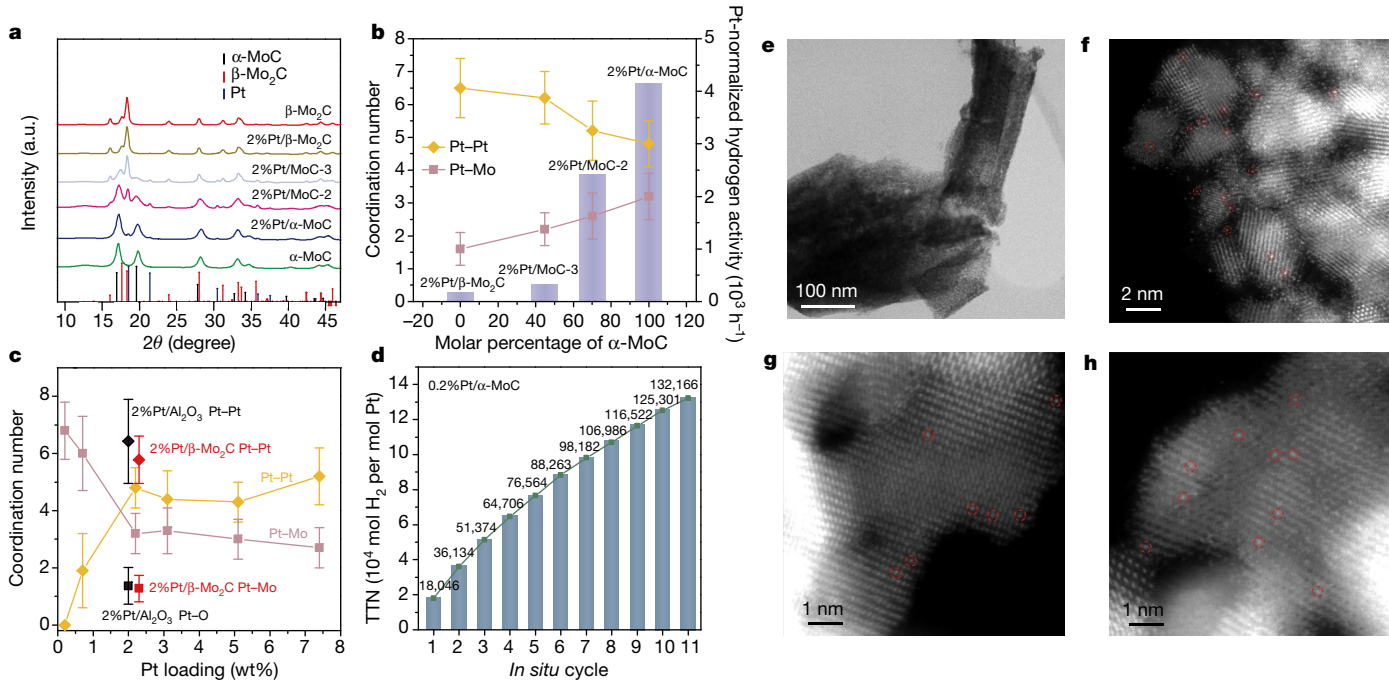


**Figure 1 | Structure and catalytic performance of Pt/MoC catalysts.**

**a**, XRD profiles, showing intensity of diffraction versus  $2\theta$  angle, for  $2\%\text{Pt}/\alpha\text{-MoC}$ ,  $2\%\text{Pt}/\text{MoC-2}$ ,  $2\%\text{Pt}/\text{MoC-3}$ ,  $2\%\text{Pt}/\beta\text{-Mo}_2\text{C}$  and pure-phase  $\alpha\text{-MoC}$  and  $\beta\text{-Mo}_2\text{C}$ . Pt,  $\alpha\text{-MoC}$  and  $\beta\text{-Mo}_2\text{C}$  are found in the Inorganic Crystal Structure Database (<https://icsd.fiz-karlsruhe.de>) under accession numbers 649490, 618306 and 618291, respectively. a.u., arbitrary units. **b**, The coordination numbers of Pt–Pt and Pt–Mo shells (data, left axis) and their catalytic activity (bars, right axis, shown as normalized hydrogen-production activity) change with the molar percentage of  $\alpha\text{-MoC}$  in Pt/MoC samples. We carried out three parallel

reactions and show here the average activity (error bars represent the standard deviation). **c**, Coordination numbers as a function of Pt loadings in Pt/ $\alpha\text{-MoC}$  catalysts. Error bars represent the fitting error of coordination numbers from EXAFS. **d**, Approaching ‘real’ APRM on  $0.2\%\text{Pt}/\alpha\text{-MoC}$  ( $n(\text{CH}_3\text{OH}):n(\text{H}_2\text{O}) = 1:1$ ). TTN, total turnover number. **e**, Low-magnification STEM bright-field image of  $2\%\text{Pt}/\alpha\text{-MoC}$ . **f**, High-resolution STEM Z-contrast image of  $2\%\text{Pt}/\alpha\text{-MoC}$ , with the single Pt atoms circled. **g**, **h**, High-resolution STEM Z-contrast images of fresh (**g**) and used (**h**)  $0.2\%\text{Pt}/\alpha\text{-MoC}$  catalyst.

easy to operate and sustainable. Also encouraging is that selectivity for the by-product carbon monoxide was low (less than 0.1%), such that it could be easily removed<sup>22,23,24</sup>. In an 11-cycle test, the  $0.2\%\text{Pt}/\alpha\text{-MoC}$  catalyst achieved a total turnover number of more than 132,000 for each platinum atom, generating about 1.68 mol hydrogen per gram catalyst (Fig. 1d). The long-term stability of the catalyst is of course important and remains to be examined and optimized, but the initial hydrogen-production activity of the system meets the requirements for state-of-the-art PEMFC vehicle applications (see Methods)<sup>25</sup>.

The interplay between platinum and  $\alpha\text{-MoC}$  has an irreplaceable role in methanol reforming. To obtain insights into the structural origins of the observed excellent catalytic performance, we characterized the catalysts fully by several methods. Atomic-resolution scanning transmission electron microscopy (STEM) Z-contrast images of  $2\%\text{Pt}/\alpha\text{-MoC}$  confirm the existence of a high density of atomically dispersed platinum atoms ( $\text{Pt}_1$ , highlighted in red) over the fcc structure of the  $\alpha\text{-MoC}$  surface (Fig. 1f and Extended Data Fig. 2). The occasionally observed platinum nanoparticles contribute directly to the metallic platinum peaks detected by XRD (Fig. 1a,  $2\%\text{Pt}/\alpha\text{-MoC}$ ). Notably, the  $0.2\%\text{Pt}/\alpha\text{-MoC}$  catalyst (which has the highest ATOF) shows predominantly atomically dispersed platinum species (Fig. 1g), and no platinum particle was observed by either STEM or XRD (Extended Data Fig. 3a); the density of  $\text{Pt}_1$  here is estimated to be about ten platinum atoms per  $100 \text{ nm}^2$ . The atomic dispersion of platinum atoms is maintained, and there is no sign of phase oxidation on the spent catalyst (Fig. 1h, Extended Data Figs 3a and 4a, b).

We then used extended X-ray-absorption fine-structure (EXAFS) analysis to determine the nature of the different platinum species. For the  $2\%\text{Pt}/\alpha\text{-MoC}$  catalysts, there is a monotonic decrease in the coordination number for platinum–platinum interactions (from 6.5 to 4.8), and an increase in the platinum–molybdenum coordination

number (from 1.6 to 3.2), as the molar percentage of  $\alpha\text{-MoC}$  in the support increases—suggesting that platinum interacts much more strongly with  $\alpha\text{-MoC}$  than with  $\beta\text{-Mo}_2\text{C}$  (Fig. 1b, Extended Data Table 1 and Extended Data Fig. 1)<sup>26</sup>. The large platinum–molybdenum coordination number could result from the atomic dispersion of platinum atoms on the  $\alpha\text{-MoC}$  surface (the  $\text{Pt}_1$  arrangement observed by STEM), while the platinum–platinum scattering is contributed mainly by the small number of platinum nanoparticles (Fig. 1a). We observe that, when the platinum loading decreases to 0.2%, the platinum–platinum coordination number drops to 0 (Fig. 1c and Extended Data Fig. 5), indicating that platinum nanoparticles are eliminated from the catalyst and that atomically dispersed platinum species become the dominant structure—in good agreement with our STEM observations.

In addition, the interaction between metal and support substantially changes the electronic structure<sup>27</sup> of platinum and  $\alpha\text{-MoC}$  in the Pt/ $\alpha\text{-MoC}$  catalyst. The binding energy of  $\text{Pt } 4f_{7/2}$  of  $0.2\%\text{Pt}/\alpha\text{-MoC}$  and  $2\%\text{Pt}/\alpha\text{-MoC}$  in X-ray photoelectron spectroscopy (XPS) experiments is 71.8 eV (Extended Data Fig. 6), which is about 0.6 eV higher than that of metallic platinum<sup>28</sup>. Indeed, when platinum is incorporated onto the surface of  $\alpha\text{-MoC}$ , density functional theory (DFT) calculations show that the electron density at platinum sites reduces greatly as compared with the density over metallic platinum, while the platinum–molybdenum interface forms electron-rich regions (Extended Data Fig. 7), thus changing the reactivity of the construct. The low ATOF of  $2\%\text{Pt}/\text{oxide}$  catalysts, which are dominated by platinum nanoparticles, indicates that these nanoparticles have only mild APRM activity. In addition, increasing the platinum loading in the Pt/ $\alpha\text{-MoC}$  catalysts leads to an increase in platinum nanoparticles and decrease in the ATOF (Extended Data Fig. 3b, c). All of these results indicate that atomically dispersed platinum accommodated over an  $\alpha\text{-MoC}$  support constitutes the most active site for the APRM reaction in this catalytic system.

**Table 1 | Various Pt/MoC catalysts and conventional platinum catalysts for generating hydrogen through APRM**

Entry*	Catalyst	Pt loading (wt%)†	Temperature (°C)	ATOF‡ (mol H <sub>2</sub> per mol Pt per hour)	H <sub>2</sub> production rate (μmol H <sub>2</sub> per gram catalyst per second)	CO (selectivity) (%)
1	2%Pt/α-MoC	2.2	190	4,134	129.6	0.06
2	2%Pt/α-MoC	2.0	170	1,755	50.0	0.07
3	2%Pt/α-MoC	2.0	150	541	15.4	0.01
4	0.2%Pt/α-MoC	0.29	190	18,046	76.2	0.14
5	2%Pt/MoC-2	2.0	190	2,402	68.4	0.05
6	2%Pt/MoC-3	2.3	190	318	10.6	—
7	2%Pt/β-Mo <sub>2</sub> C	2.1	190	168	5.0	0.13
8	2%Pt/Al <sub>2</sub> O <sub>3</sub>	2.0	190	171	4.9	0.07
9	2%Pt/TiO <sub>2</sub>	2.0	190	148	4.2	0.02
10	α-MoC	—	190	—	2.3	0.83
11	2%Pt/α-MoC§	2.0	190	1,020	29.0	—
12	2%Pt/α-MoC**	2.0	190	699	20.0	0.12

\*Reaction conditions:  $n(\text{CH}_3\text{OH}):n(\text{H}_2\text{O}) = 1:3$  (except for entries 4, 11 and 12), 50 ml total volume of liquid, 100 mg catalysts, 190 °C; reaction for 1.25 hours; 2 MPa N<sub>2</sub> (10% Ar as internal standard).

†Pt loadings were measured by inductively coupled plasma atomic emission spectrometry (ICP-AES).

‡The turnover frequency was averaged over 1.25 hours.

|| $n(\text{CH}_3\text{OH}):n(\text{H}_2\text{O}) = 1:1$ .

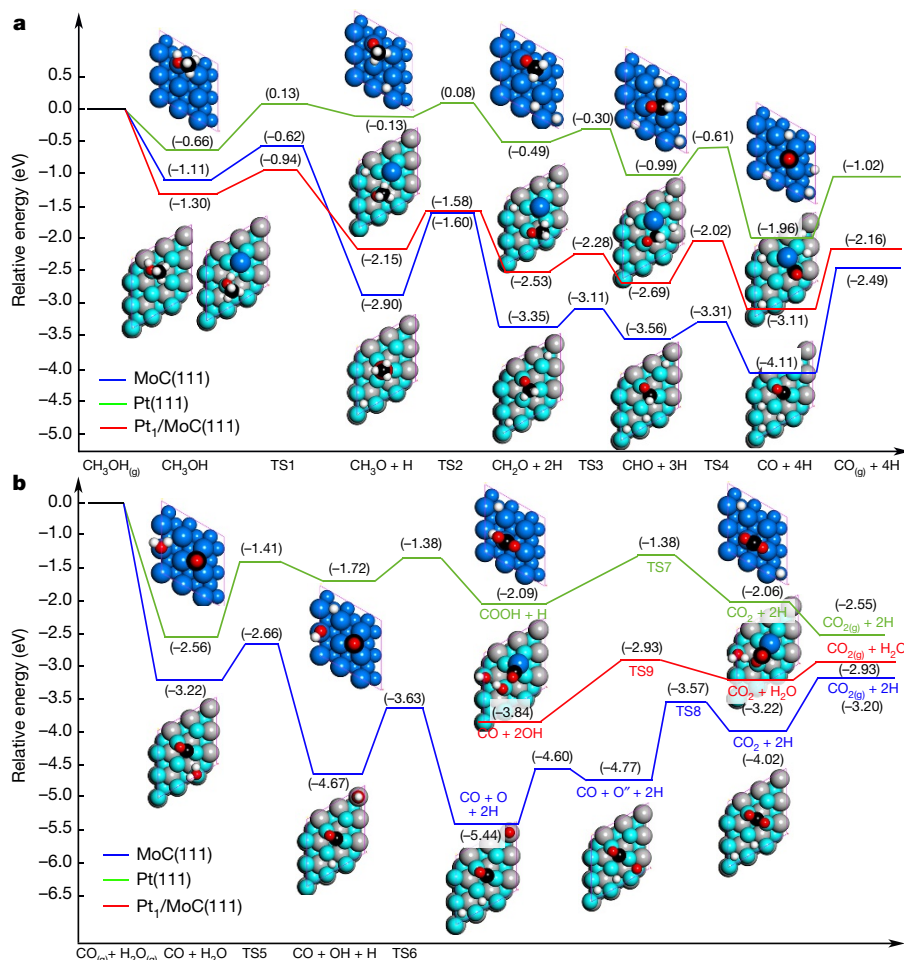
||Pure α-MoC without Pt content.

§The reactant was ethanol:  $n(\text{CH}_3\text{CH}_2\text{OH}):n(\text{H}_2\text{O}) = 1:3$ .

\*\*The reactant was ethylene glycol:  $n(\text{HOCH}_2\text{CH}_2\text{OH}):n(\text{H}_2\text{O}) = 1:3$ .

We further carried out first-principle calculations to investigate the structural and electronic properties of the Pt/α-MoC catalyst, as well as the reaction mechanism. On the basis of our experimental characterization results, we constructed three catalyst models (Extended Data Fig. 7a) to represent the different active sites in Pt/α-MoC: molybdenum-terminated α-MoC(111); Pt(111), to simulate platinum nanoparticles; and Pt<sub>1</sub>/α-MoC, to model atomically dispersed platinum over α-MoC(111).

DFT calculations confirm that the special geometric and electronic properties resulting from the strong interaction between platinum and α-MoC benefit the APRM reaction. Electrons are donated from platinum to α-MoC (Extended Data Figs 1h, 4c and 6), and the electron-deficient Pt<sub>1</sub> sites have lower affinity for carbon monoxide than does the Pt(111) surface (Extended Data Fig. 8). Detailed reaction-pathway calculations show that the decomposition of methanol into methoxyl and the dissociation of water are thermodynamically favoured on pure

**Figure 2 | Reaction path for hydrogen production from methanol and water.**

**a**, Energy profiles for CH<sub>3</sub>OH dissociation into CO and H atoms on α-MoC(111), Pt(111) and Pt<sub>1</sub>/α-MoC(111) surfaces. The x axis shows the reaction intermediates and transition states (TSs); the y axis shows the relative energy of each state. **b**, Energy profiles for CO<sub>2</sub> formation via the water-gas shift reaction on these three surfaces. Pt, Mo, C, O and H atoms are shown in blue, cyan, grey, red and white, respectively; in order to make a distinction, the C atoms from CH<sub>3</sub>OH are in dark blue. O'' refers to oxygen on a different adsorption site with respect to the previous state; a subscript 'g' denotes a gas-phase reactant or product.

**Table 2 | Effective energy barriers and reactive sites for water dissociation and methanol decomposition on various catalysts**

Catalyst	$\text{H}_2\text{O} \rightarrow \text{OH} + \text{H}$		$\text{CH}_3\text{OH} \rightarrow \text{CO} + 4\text{H}$		Water-gas shift reaction		Rate constant ratio $(k_{\text{H}_2\text{O}}/k_{\text{CH}_3\text{OH}})^*$	
	$E_a$ (eV)	Site	$E_a$ (eV)	Site	$E_a$ (eV)	Site		
MoC	0.56	MoC	1.30	MoC	1.87	No	$6.56 \times 10^8$	
Pt(111)	1.15	Pt	0.79	Pt	1.18	No	$5.13 \times 10^{-5}$	
Pt <sub>1</sub> /MoC	0.56	MoC	0.67	Interface	0.91	Interface	20.44	

The effective barrier is the activation energy ( $E_a$ ) of a series of elementary steps, and is the energy between the most stable state and the highest transition state.

\*This is the rate constant ratio between water and methanol dissociation.

$\alpha$ -MoC(111) (Fig. 2, Table 2 and Extended Data Fig. 9), with energy barriers of 0.49 eV and 0.56 eV, respectively. However, the further dehydrogenation of methoxyl groups is kinetically hindered under moderate conditions, owing to the high barrier for the subtraction of C–H bonds (1.30 eV). On the other hand, over Pt(111), although methanol could be effectively activated (the effective barrier is 0.79 eV), water dissociation and the substantial reforming of CO\* cannot proceed at low temperatures (effective barrier of 1.18 eV). Notably, on the Pt<sub>1</sub>/ $\alpha$ -MoC(111) bifunctional catalyst, in which there are sites for scissoring O–H bonds (on  $\alpha$ -MoC next to Pt<sub>1</sub>) and C–H bonds (Pt<sub>1</sub>), the barrier for complete dissociation of methanol to CO\*/H\* is reduced to 0.67 eV, and the rate-limiting step is the dissociation of the last C–H bond. The adsorbed carbon monoxide (on Pt<sub>1</sub>) further reforms with hydroxyl groups at the interface with  $\alpha$ -MoC, with a barrier of 0.91 eV, agreeing well with the experimental apparent activation energy of 0.86 eV (Extended Data Fig. 3d). The synergy between Pt<sub>1</sub> and  $\alpha$ -MoC—and the bifunctional nature of Pt/ $\alpha$ -MoC—gives this catalyst exceptional low-temperature catalytic activity (Table 2), as confirmed in temperature-programmed surface reaction experiments (Extended Data Fig. 10).

We have developed a new catalyst that comprises atomically dispersed platinum over  $\alpha$ -MoC. This catalyst shows outstanding hydrogen-production activity and stability in the low-temperature APRM process. The  $\alpha$ -MoC provides highly active sites for water dissociation (with an activation energy of 0.56 eV), producing abundant surface hydroxyls and thus accelerating the methanol-reforming reaction at the interface between Pt<sub>1</sub> and  $\alpha$ -MoC. Meanwhile, the well dispersed Pt<sub>1</sub> geometry maximizes the exposed active interface of Pt<sub>1</sub>/ $\alpha$ -MoC and effectively increases the density of active sites for the reforming reaction. This new catalyst paves the way towards a commercially achievable hydrogen-storage strategy.

**Online Content** Methods, along with any additional Extended Data display items and Source Data, are available in the online version of the paper; references unique to these sections appear only in the online paper.

Received 14 October 2015; accepted 19 January 2017.

Published online 22 March 2017.

- Steele, B. C. & Heinzel, A. Materials for fuel-cell technologies. *Nature* **414**, 345–352 (2001).
- Schlappbach, L. & Zettel, A. Hydrogen-storage materials for mobile applications. *Nature* **414**, 353–358 (2001).
- Amphlett, J. C. *et al.* Hydrogen-production by steam reforming of methanol for polymer electrolyte fuel-cells. *Int. J. Hydrogen Energy* **19**, 131–137 (1994).
- David, W. I. *et al.* Hydrogen production from ammonia using sodium amide. *J. Am. Chem. Soc.* **136**, 13082–13085 (2014).
- Yu, K. M. K. *et al.* Non-syngas direct steam reforming of methanol to hydrogen and carbon dioxide at low temperature. *Nat. Commun.* **3**, 1230 (2012).
- Lee, J. K., Ko, J. B. & Kim, D. H. Methanol steam reforming over Cu/ZnO/Al<sub>2</sub>O<sub>3</sub> catalyst: kinetics and effectiveness factor. *Appl. Catal. A Gen.* **278**, 25–35 (2004).
- Sá, S., Silva, H., Brandão, L., Sousa, J. M. & Mendes, A. Catalysts for methanol steam reforming—a review. *Appl. Catal. B* **99**, 43–57 (2010).
- Setthapun, W., Bej, S. K. & Thompson, L. T. Carbide and nitride supported methanol steam reforming catalysts: parallel synthesis and high throughput screening. *Top. Catal.* **49**, 73–80 (2008).

- Davda, R. R., Shabaker, J. W., Huber, G. W., Cortright, R. D. & Dumesic, J. A. A review of catalytic issues and process conditions for renewable hydrogen and alkanes by aqueous-phase reforming of oxygenated hydrocarbons over supported metal catalysts. *Appl. Catal. B* **56**, 171–186 (2005).
- Song, C. Fuel processing for low-temperature and high-temperature fuel cells: challenges and opportunities for sustainable development in the 21st century. *Catal. Today* **77**, 17–49 (2002).
- Deng, Z.-Y., Ferreira, J. M. F. & Sakka, Y. Hydrogen-generation materials for portable applications. *J. Am. Ceram. Soc.* **91**, 3825–3834 (2008).
- Cortright, R. D., Davda, R. R. & Dumesic, J. A. Hydrogen from catalytic reforming of biomass-derived hydrocarbons in liquid water. *Nature* **418**, 964–967 (2002).
- Shabaker, J. W., Davda, R. R., Huber, G. W., Cortright, R. D. & Dumesic, J. A. Aqueous-phase reforming of methanol and ethylene glycol over alumina-supported platinum catalysts. *J. Catal.* **215**, 344–352 (2003).
- Nielsen, M. *et al.* Low-temperature aqueous-phase methanol dehydrogenation to hydrogen and carbon dioxide. *Nature* **495**, 85–89 (2013).
- Gunalanathan, C. & Milstein, D. Bond activation and catalysis by ruthenium pincer complexes. *Chem. Rev.* **114**, 12024–12087 (2014).
- Denard, C. A. *et al.* Cooperative tandem catalysis by an organometallic complex and a metalloenzyme. *Angew. Chem. Int. Ed.* **126**, 475–479 (2014).
- Qiao, B. T. *et al.* Single-atom catalysis of CO oxidation using Pt<sub>1</sub>/FeO<sub>x</sub>. *Nat. Chem.* **3**, 634–641 (2011).
- Zhai, Y. *et al.* Alkali-stabilized Pt-OH<sub>x</sub> species catalyze low-temperature water-gas shift reactions. *Science* **329**, 1633–1636 (2010).
- Zhao, D. & Xu, B. Q. Enhancement of Pt utilization in electrocatalysts using gold nanoparticles. *Angew. Chem. Int. Ed.* **45**, 4955–4959 (2006).
- Fu, Q., Saltsburg, H. & Flytzani-Stephanopoulos, M. Active nonmetallic Au and Pt species on ceria-based water-gas shift catalysts. *Science* **301**, 935–938 (2003).
- Yang, M. *et al.* Catalytically active Au-O(OH)<sub>x</sub>-species stabilized by alkali ions on zeolites and mesoporous oxides. *Science* **346**, 1498–1501 (2014).
- Li, J. *et al.* Direct conversion of cellulose using carbon monoxide and water on a Pt-Mo<sub>2</sub>C/C catalyst. *Energy Environ. Sci.* **7**, 393–398 (2014).
- Lebarbier, V. M. *et al.* Sorption-enhanced synthetic natural gas (SNG) production from syngas: a novel process combining CO methanation, water-gas shift, and CO<sub>2</sub> capture. *Appl. Catal. B* **144**, 223–232 (2014).
- Fu, Q. *et al.* Interface-confined ferrous centers for catalytic oxidation. *Science* **328**, 1141–1144 (2010).
- US Department of Energy. *Compare Fuel Cell Vehicles* [http://www.fueleconomy.gov/feg/fcv\\_sbs.shtml](http://www.fueleconomy.gov/feg/fcv_sbs.shtml) (accessed 19 January 2017).
- Schweitzer, N. M. *et al.* High activity carbide supported catalysts for water gas shift. *J. Am. Chem. Soc.* **133**, 2378–2381 (2011).
- Wei, H. *et al.* FeO<sub>x</sub>-supported platinum single-atom and pseudo-single-atom catalysts for chemoselective hydrogenation of functionalized nitroarenes. *Nat. Commun.* **5**, 5634 (2014).
- Moulder, J. F., Chastain, J. & King, R. C. *Handbook of X-ray Photoelectron Spectroscopy: A Reference Book of Standard Spectra For Identification and Interpretation of XPS Data* (Perkin-Elmer, 1992).

**Acknowledgements** We received financial support from the 973 Project (grants 2011CB201402 and 2013CB933100) and the Natural Science Foundation of China (grants 91645115, 21473003, 91645115, 21222306, 21373037, 21577013 and 91545121). The electron-microscopy work was supported in part by the Chinese Academy of Sciences (CAS) Pioneer Hundred Talents Program; by the US Department of Energy (DOE), Office of Science, Basic Energy Science, Materials Sciences and Engineering Division (to W.Z.); and through a user project at Oak Ridge National Laboratory's Center for Nanophase Materials Sciences (CNMS), which is a DOE Office of Science User Facility. The XAS experiments were conducted in the Shanghai Synchrotron Radiation Facility (SSRF) and Beijing Synchrotron Radiation Facility (BSRF). This research used Beamline 17-BM of the Advanced Photon Source (APS), a US DOE Office of Science User Facility operated for the DOE Office of Science by Argonne National Laboratory under contract no. DE-AC02-06CH11357 (to W.X.). We also acknowledge National Thousand Young Talents Program of China—the CAS Hundred Talents Program and the Shanxi Hundred Talent Program.

**Author Contributions** D.M. designed the study. L.L. performed most of the reactions. W.Z. and S.Z. performed the electron-microscopy characterization and proposed the structural model for the active sites. C.S. and X.Z. synthesized part of the molybdenum carbides. R.G., Y.-W.L. and X.-D.W. finished the DFT calculations. S.Y., W.X. and Z.J. carried out the X-ray structure characterization and analysis. L.L., D.M., X.-D.W., S.Y., C.S. and W.Z. wrote the paper. The other authors provided reagents, performed some of the experiments and revised the paper.

**Author Information** Reprints and permissions information is available at [www.nature.com/reprints](http://www.nature.com/reprints). The authors declare competing financial interests: details are available in the online version of the paper. Readers are welcome to comment on the online version of the paper. Publisher's note: Springer Nature remains neutral with regard to jurisdictional claims in published maps and institutional affiliations. Correspondence and requests for materials should be addressed to D.M. (dma@pku.edu.cn), X.-D.W. (wxd@sxicc.ac.cn) or C.S. (chuansi@dlutedu.edu.cn).

**Reviewer Information** *Nature* thanks D. Vlachos and the other anonymous reviewer(s) for their contribution to the peer review of this work.

## METHODS

**Preparation of catalysts.**  $\alpha\text{-MoC}$  support. Ammonium paramolybdate ( $(\text{NH}_4)_6\text{Mo}_7\text{O}_{24} \cdot 4\text{H}_2\text{O}$ ) was purchased from Sinopharm Chemical Reagent Co. Ltd. A grinded powder of ammonium paramolybdate was calcined in a muffle oven to 500 °C at a rate of 10 °C min<sup>-1</sup> to synthesize the precursor MoO<sub>3</sub>. Then 0.8 g MoO<sub>3</sub> was loaded into a quartz tube reactor and placed in a vertical furnace. The powder was heated to 700 °C in NH<sub>3</sub> (100 ml min<sup>-1</sup>; pre-purified gas) at a rate of 5 °C min<sup>-1</sup> and kept at 700 °C for 2 hours. After the sample was cooled to room temperature, the gas was then switched to a CH<sub>4</sub>/H<sub>2</sub> mixture (100 ml min<sup>-1</sup>; 20/80 v/v), and the temperature was increased to 700 °C at 5 °C min<sup>-1</sup> and held at 700 °C for 2 hours. Finally, the sample was passivated at room temperature using a 0.5% O<sub>2</sub>/He gas mixture<sup>29</sup>. Elemental analysis finds that the Mo/C ratio of  $\alpha\text{-MoC}$  is around 1/0.8.

$\beta\text{-Mo}_2\text{C}$  support.  $\beta\text{-Mo}_2\text{C}$  was synthesized using the same precursor as  $\alpha\text{-MoC}$ , as follows: 0.8 g MoO<sub>3</sub> was loaded in the quartz tube and carburized with a CH<sub>4</sub>/H<sub>2</sub> mixture (100 ml min<sup>-1</sup>; 20/80 v/v), with the temperature being increased at 5 °C min<sup>-1</sup> to 300 °C, then at 1 °C min<sup>-1</sup> to 700 °C. After carburization at 700 °C for 2 hours, the sample was cooled to room temperature and passivated using a 0.5% O<sub>2</sub>/He gas mixture.

2%Pt/ $\beta\text{-Mo}_2\text{C}$  catalyst. The passivated  $\beta\text{-Mo}_2\text{C}$  support was transferred to a deaerated, aqueous solution containing an appropriate amount of chloroplatinic acid (H<sub>2</sub>PtCl<sub>6</sub>•6H<sub>2</sub>O) to achieve the desired loading. The slurry was stirred for 3 hours, dried using evaporation, and then transferred to a freeze dryer overnight to remove any moisture. Before catalytic evaluation, the catalyst was activated with a CH<sub>4</sub>/H<sub>2</sub> mixture (15/85 v/v). The activation temperature program heated the sample to 300 °C and held it there for 1 hour. The temperature was then increased to 590 °C at a rate of 5 °C min<sup>-1</sup> and held there for another 2 hours.

2%Pt/ $\alpha\text{-MoC}$  and 2%Pt/MoC-2 catalysts. An appropriate amount of H<sub>2</sub>PtCl<sub>6</sub>•6H<sub>2</sub>O was loaded onto a homemade MoO<sub>3</sub> support, using a wetness impregnation method. (To synthesize MoO<sub>3</sub>, an appropriate amount of ammonium paramolybdate was dissolved into pure water, adjusting the pH of the solution to 3.7. The solution underwent ultrasonication for 2 hours. The precipitates thus generated were separated by evaporation of solvent and dried at 60 °C under a vacuum overnight. The precipitates were then grinded into powder and calcined in air at 500 °C for 4 hours.) After being dried at room temperature under vacuum, the sample was calcined at 500 °C for 4 hours. For Pt/ $\alpha\text{-MoC}$ , the calcined Pt/MoO<sub>3</sub> was carburized using the same procedure as for the synthesis of  $\beta\text{-Mo}_2\text{C}$ . For Pt/MoC-2, MoO<sub>3</sub> impregnated with H<sub>2</sub>PtCl<sub>6</sub> was carburized directly without calcination in air at 500 °C.

2%Pt/MoC-3 catalysts. An appropriate amount of H<sub>2</sub>PtCl<sub>6</sub>•6H<sub>2</sub>O aqueous solution was added into the ammonium paramolybdate solution dropwise under stirring. A yellow precipitant was thus generated. The solvent was evaporated at 90 °C and the precipitant was dried at 120 °C for 3 hours to ensure that the powder was dried<sup>30</sup>. Then the sample was carburized (as for  $\beta\text{-Mo}_2\text{C}$ ) directly to obtain 2%Pt/MoC-3. 2%Pt/Al<sub>2</sub>O<sub>3</sub> and 2%Pt/TiO<sub>2</sub>. These reference catalysts were synthesized using wet impregnation of H<sub>2</sub>PtCl<sub>6</sub>•6H<sub>2</sub>O over commercial Al<sub>2</sub>O<sub>3</sub> and TiO<sub>2</sub> supports<sup>12</sup>. The slurry was stirred for 3 hours in air to remove the liquid, using the rotary evaporator under vacuum at 35 °C. The material was dried at 120 °C for 3 hours, and then calcined in the muffle oven at 500 °C. The Pt loading is 2%. The catalysts were reduced with H<sub>2</sub> before catalytic evaluation.

Pt/ $\alpha\text{-MoC}$  catalysts with different Pt loadings. Pt/ $\alpha\text{-MoC}$  catalysts with 2.2 wt%, 3.1 wt%, 5.1 wt% and 7.4 wt% Pt loadings were prepared as for Pt/ $\alpha\text{-MoC}$ . Samples with 0.2 wt% and 0.7 wt% Pt loading were prepared using the wetness impregnation method with activated  $\alpha\text{-MoC}$  as the support. The catalysts are denoted  $x\text{wt}\%$  Pt/ $\alpha\text{-MoC}$ , where  $x$  denotes the rough weight concentration of Pt ( $x = 0.2, 1, 2, 3, 5$  or 7).

**Evaluation of catalytic performance.** Before their performance was evaluated, all Pt/MoC catalysts were activated in a CH<sub>4</sub>/H<sub>2</sub> mixture (15/85 v/v) at 590 °C for 2 hours. The Pt/oxide catalysts were activated in H<sub>2</sub> flow at 500 °C. After being cooled to room temperature, the activated sample was transferred into de-aerated water in the autoclave under the protection of a N<sub>2</sub> flow. The sealed autoclave was purged using 2 MPa N<sub>2</sub> (10 vol% Ar was used as an internal standard) three times. The catalytic reactions were carried out at 190 °C (the pressure of the system was as high as 6 MPa), and after the reaction the gas phase was analysed using an Agilent 7820 gas chromatograph with a thermal conductivity detector (TCD). We quantified the gas-phase concentration of H<sub>2</sub>, CO and CH<sub>4</sub>; however, we could not accurately determine the concentration of CO<sub>2</sub> owing to its high solubility in the liquid phase, especially at high pressures. We analysed the liquid-phase products on an Agilent HPLC 1200 using a Prevail carbohydrate ES 5-μm column. To generate the results shown in Fig. 1d, for each cycle, the system was reacted at 190 °C for 1.25 hours. After cooling down to room temperature, the gases were analysed by gas chromatography and then released. Then the system was reheated to 190 °C

and reacted for another 1.25-hour cycle. A total of 11 cycles was conducted, with the turnover number reaching 132,166. As regards the observed decline in turnover number per cycle, the possible reasons could be: first, some catalyst particles migrated to the upper part of the reactor during the reaction; or second, the CO<sub>2</sub> accumulating in the liquid partially suppressed the reaction.

We measured the activity in the methanol (or ethanol or ethylene glycol)-reforming reaction through the amount of H<sub>2</sub> produced in a certain reaction time. We determined this amount using internal standards and according to the following equations:

$$\begin{aligned} n_{\text{H}_2} &= f_{\text{H}_2} A_{\text{H}_2} \frac{n_{\text{Ar}}}{n_{\text{Ar}} n_{\text{H}_2}} \\ S_{\text{CO}} &= n_{\text{CO}} / n_{\text{H}_2} \\ S_{\text{CH}_4} &= n_{\text{CH}_4} / n_{\text{H}_2} \end{aligned} \quad (1)$$

where  $n_x$  is the molar concentration of gas  $x$ ;  $f_x$  is the response factor of gas  $x$ , calibrated using a mixture of standards;  $A_x$  is the measured peak area of gas  $x$ ; and  $S_x$  is the selectivity for the by-products CO and CH<sub>4</sub>. The amount of Ar ( $n_{\text{Ar}}$ ) is determined from the partial pressure of Ar (0.2 MPa) and the volume of the autoclave (135 ml; the liquid occupies 50 ml of this) using the ideal gas equation. The amount of hydrogen product was determined on the basis of equation (1). The selectivity for by-products is defined as the molar ratio of the by-product to the main product, H<sub>2</sub>, in the gas phase.

**Estimation of Pt usage for a commercial PEMFC vehicle.** The reported hydrogen consumption and range of the Toyota Mirai 2017 vehicle are 1 kg H<sub>2</sub> per 100 km (at a speed of about 100 km h<sup>-1</sup>; ref. 25) and 500 km, respectively.

To fuel such a vehicle, we propose using hydrogen-reforming stacks to replace high-pressure hydrogen-storage tanks. Methanol and water would be stored separately. Given that the hydrogen fuel cell produces pure water, the water is recyclable. The fuel tank used in traditional cars could be filled with methanol.

Whether this strategy would work in practice is a complicated problem that is related to both science and engineering. Here, we roughly estimate the amount of our 0.2%Pt/ $\alpha\text{-MoC}$  catalyst that would be required. Further engineering effort is needed in order to optimize the process and bring it to practical application. Given the hydrogen-consumption rate of Mirai (1 kg h<sup>-1</sup>) and the Pt-normalized hydrogen-production rate (18,000 mol H<sub>2</sub> per mol Pt per hour) of the 0.2%Pt/ $\alpha\text{-MoC}$  catalyst, around 6 g Pt should meet the requirements of Mirai per hour, which corresponds to approximately 3 kg of 0.2%Pt/ $\alpha\text{-MoC}$  catalyst.

**Structural characterization.** *X-ray diffraction.* The XRD measurements presented in Fig. 1 were taken at the 17-BM beamline ( $\lambda = 0.72768 \text{ \AA}$ ) of the Advanced Photon Source at Argonne National Laboratory. A 3 mg powder sample of each passivated Pt/MoC catalyst was loaded into an amorphous silica tube of diameter 1.0 mm. Two-dimensional XRD patterns were collected with a Perkin Elmer amorphous silicon detector, and the diffraction rings were integrated using the Fit2d code (<http://www.esrf.eu/computing/scientific/FIT2D>). Rietveld refinements of the measured XRD patterns were done using GSAS packages<sup>31</sup>.

XRD patterns of spent catalysts and of catalysts with different amounts of Pt loading (Extended Data Fig. 3) were collected on a Rigaku X-ray diffractometer operated at 40 kV and 100 mA, using Cu K $\alpha$  radiation.

*X-ray-absorption fine structure.* Molybdenum K-edge (20,000 eV) XAFS spectra were measured at the BL14W beamline of the Shanghai Synchrotron Radiation Facility in transmission mode, using an ion chamber as the detector. Mo foil, MoO<sub>2</sub> (Aldrich) and MoO<sub>3</sub> (Aldrich) were used as standards. Before measurement, all of the samples were activated in a mixture of CH<sub>4</sub> and H<sub>2</sub> (20/80 v/v) at 590 °C for 2 hours and carefully sealed under argon protection in a glove box.

Platinum L<sub>3</sub>-edge (11,564 eV) XAFS spectra were also measured at the BL14W beamline, in fluorescence mode, using a Lytle detector to collect the data. For samples with low metal loading (less than 1%), a 32-channel solid detector was used and multiple parallel scans were applied to achieve high data quality. Pt foil and PtO<sub>2</sub> (Adamas-beta) were used as standards. The XAFS samples were sealed in a chamber with Kapton windows under argon protection in a glove box after activation.

All XAFS spectra were processed using the Ifeffit package<sup>32</sup>. The extended XAFS oscillation was fitted according to a back-scattering equation, using FEFF models<sup>32</sup> generated from crystal structures of MoC (space group Fm $\bar{3}m$ ), Mo<sub>2</sub>C (P63/mmc) and Pt (Fm $\bar{3}m$ ).

*X-ray photoelectron spectroscopy.* XPS spectra for activated 2%Pt/ $\alpha\text{-MoC}$  and 0.2%Pt/ $\alpha\text{-MoC}$  catalysts were collected using an Axis ultraimaging photo-electron spectrometer (Kratos Analytical). The passivated catalyst fine powder was made into a small pellet (6 mm diameter) and held on the sample holder. This pellet was then activated in the pretreatment chamber of the XPS spectrometer

under a  $60\text{ ml min}^{-1}$  flow of 15%  $\text{CH}_4/\text{H}_2$  at  $590^\circ\text{C}$  for 2 hours. After activation, the sample was introduced directly into an ultrahigh-vacuum chamber for XPS measurement at room temperature without exposure to air. The XPS spectra were processed using CasaXPS software (<http://www.casaxps.com/>).

To investigate the surface chemical structure of catalyst after exposure to methanol and water, we activated the pellet of 2%Pt/ $\alpha$ -MoC or 0.2%Pt/ $\alpha$ -MoC in the pretreatment chamber of the XPS spectrometer at  $590^\circ\text{C}$  under  $60\text{ ml min}^{-1}$   $\text{CH}_4/\text{H}_2$  for 2 hours. After collecting the spectra, we exposed the activated sample to  $60\text{ ml min}^{-1}$  methanol (0.8 kPa)/water (2.3 kPa)/ $\text{N}_2$  for 60 min at  $190^\circ\text{C}$ . After exposure, the catalyst pellet was transferred into the ultrahigh-vacuum chamber for measurement.

**Electron microscopy.** STEM characterization was performed on an aberration-corrected Nion UltraSTEM-100, operated at  $100\text{ kV}$  (ref. 33). The Z-contrast images were collected with an annular dark field detector in the range of  $86\text{--}200\text{ mrad}$ . The convergence angle was set to  $30\text{ mrad}$ . Electron energy-loss spectroscopy was carried out with the same experimental set-up.

Catalyst samples for STEM analysis were prepared by first embedding the catalyst powder in resin and then slicing it into electron-transparent TEM samples using a microtome. The TEM samples were baked at  $160^\circ\text{C}$  under vacuum for 8 hours before loading them into the electron microscope. Control experiments were performed on samples prepared by dry dispersing of catalyst powder directly onto the TEM grid inside a glovebox under argon protection and without vacuum baking. The results are qualitatively the same.

**Temperature-programmed surface reactions.** *Methanol desorption.* We examined the desorption behaviour of methanol on the catalysts using the temperature-programmed desorption (TPD) technique. Before analysis, we pretreated about  $50\text{ mg}$  of the passivated Pt/MoC-based catalyst in 15%  $\text{CH}_4/\text{H}_2$  for 2 hours at  $590^\circ\text{C}$  (Pt/oxide supports were pretreated in  $\text{H}_2$  for 2 hours at  $500^\circ\text{C}$ ) in a quartz tube, and then cooled the samples to  $35^\circ\text{C}$ . Then the system was purged thoroughly with helium to remove the desorbed molecules. Saturated methanol vapour was then introduced into the system by means of a  $80\text{ ml min}^{-1}$  helium flow for 15 min from a bubbler that was maintained at  $35^\circ\text{C}$ . After methanol adsorption, the system was further purged by helium flow until no signal of desorbed methanol ( $m/z=31$ ) could be observed. The test sample was then heated to  $500^\circ\text{C}$  at a rate of  $5^\circ\text{C min}^{-1}$  under  $80\text{ ml min}^{-1}$  helium flow. Signals of  $\text{H}_2$  ( $m/z=2$ ), He ( $m/z=4$ ),  $\text{CH}_4$  ( $m/z=15$ ),  $\text{H}_2\text{O}$  ( $m/z=18$ ), CO ( $m/z=28$ ),  $\text{CH}_3\text{OH}$  ( $m/z=31$ ),  $\text{CO}_2$  ( $m/z=44$ ),  $\text{HCOOH}$  ( $m/z=45$ ),  $\text{HCHO}$  ( $m/z=30$ ) and  $\text{HCOOCH}_3$  ( $m/z=60$ ) were recorded with an OMNI Star mass spectrometer.

*Methanol plus water surface reaction.* The temperature-programmed surface reaction of methanol and water uses the same experimental procedure as that for methanol TPD, except for the adsorption stage: here, a mixture of methanol and water was introduced by  $80\text{ ml min}^{-1}$  helium flow for 15 min at room temperature. (The amount of methanol and water in the mixture was calculated from the phase diagram for the methanol–water system, and the molarity of methanol aqueous solution was controlled such that  $P_{\text{methanol}}/P_{\text{water}}$  in the gas phase equalled 1.)

**Computational details.** *Methods.* All calculations were performed using the plane-wave-based periodic DFT method, as implemented in the Vienna *ab initio* simulation package (VASP)<sup>34,35</sup>. The electron-ion interaction was described with the projector augmented wave (PAW) method<sup>36,37</sup>. The electron-exchange and -correlation energies were treated within the generalized gradient approximation in the Perdew–Burke–Ernzerhof functional (GGA-PBE)<sup>38</sup>. The plane-wave basis was set up to  $450\text{ eV}$ . Electron smearing was used via the Methfessel–Paxton technique

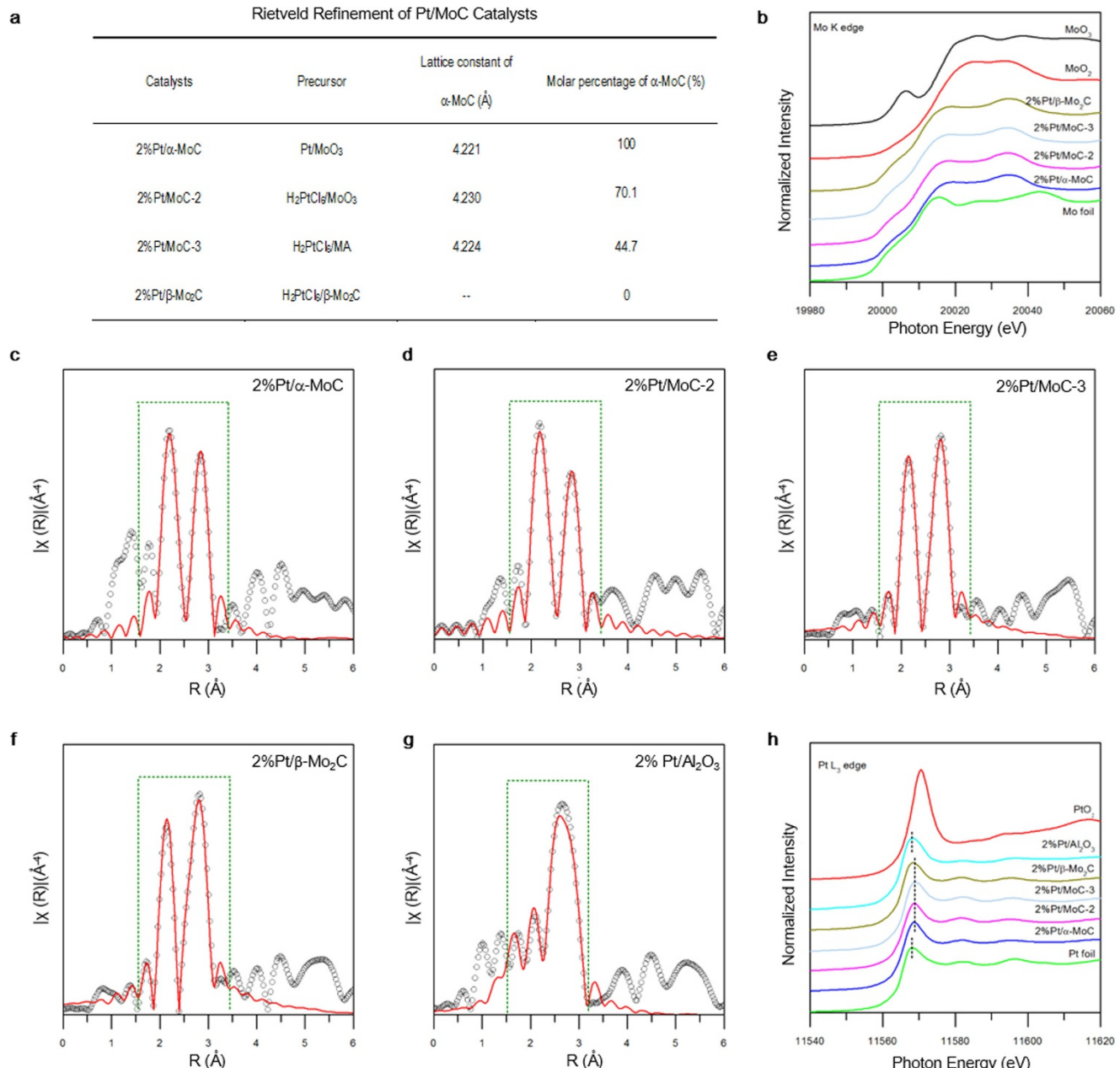
with a smearing width consistent to  $\sigma=0.2\text{ eV}$ . The adsorption energies included spin polarization. All transition states were estimated using the climbing image nudged elastic band method (CI-NEB)<sup>39</sup>, and we analysed the stretching frequencies in order to characterize whether a stationary point is a minimum state without imaginary frequency or a transition state with only one imaginary frequency. We also included the van der Waals interaction ( $D_3$ ) in this work.

We calculated the adsorption energy,  $E_{\text{ads}}$ , according to  $E_{\text{ads}} = E_{\text{X/slab}} - (E_{\text{slab}} + E_{\text{X}})$ , where  $E_{\text{X/slab}}$  is the total energy of the slab (the clean surface) with adsorbates in its equilibrium geometry,  $E_{\text{slab}}$  is the total energy of the bare slab, and  $E_{\text{X}}$  is the total energy of the free adsorbates in the gas phase. Therefore, the more negative the adsorption energy, the stronger the adsorption. The activation barrier (or activation energy,  $E_a$ ) and reaction energy ( $\Delta E_r$ ) are calculated according to  $E_a = E_{\text{TS}} - E_{\text{IS}}$  and  $\Delta E_r = E_{\text{FS}} - E_{\text{IS}}$ , where  $E_{\text{IS}}$ ,  $E_{\text{FS}}$  and  $E_{\text{TS}}$  are the energies of the corresponding initial state (IS), final state (FS) and transition state (TS), respectively.

**Models.** The calculated lattice constant of a cubic platinum cell (fcc) is  $3.9194\text{ \AA}$  (experimental constant of  $3.9239\text{ \AA}$ ), and the Pt–Pt bond has a length of  $2.771\text{ \AA}$ . The calculated lattice constant of a cubic MoC cell (fcc) is  $4.3318\text{ \AA}$  (experimental of  $4.270\text{ \AA}$ ), and the Mo–Mo bond is  $3.063\text{ \AA}$  long. For the top views of surface models for  $\alpha$ -MoC(111), Pt(111) and  $\text{Pt}_1/\alpha$ -MoC(111) (Extended Data Fig. 7), we used the same unit cell—namely  $p(3 \times 3)$ —and  $3 \times 3 \times 1$  k-point sampling. In total, the MoC(111) surface has 27 molybdenum and 27 carbon atoms, of which 9 molybdenum and 18 carbon atoms were fixed; the Pt(111) has 36 platinum atoms, and 18 of these were fixed; the  $\text{Pt}_1/\text{MoC}(111)$  has 1 platinum, 27 molybdenum and 27 carbon atoms, of which 9 molybdenum and 18 carbon atoms were fixed, and the platinum coverage was 1/9.

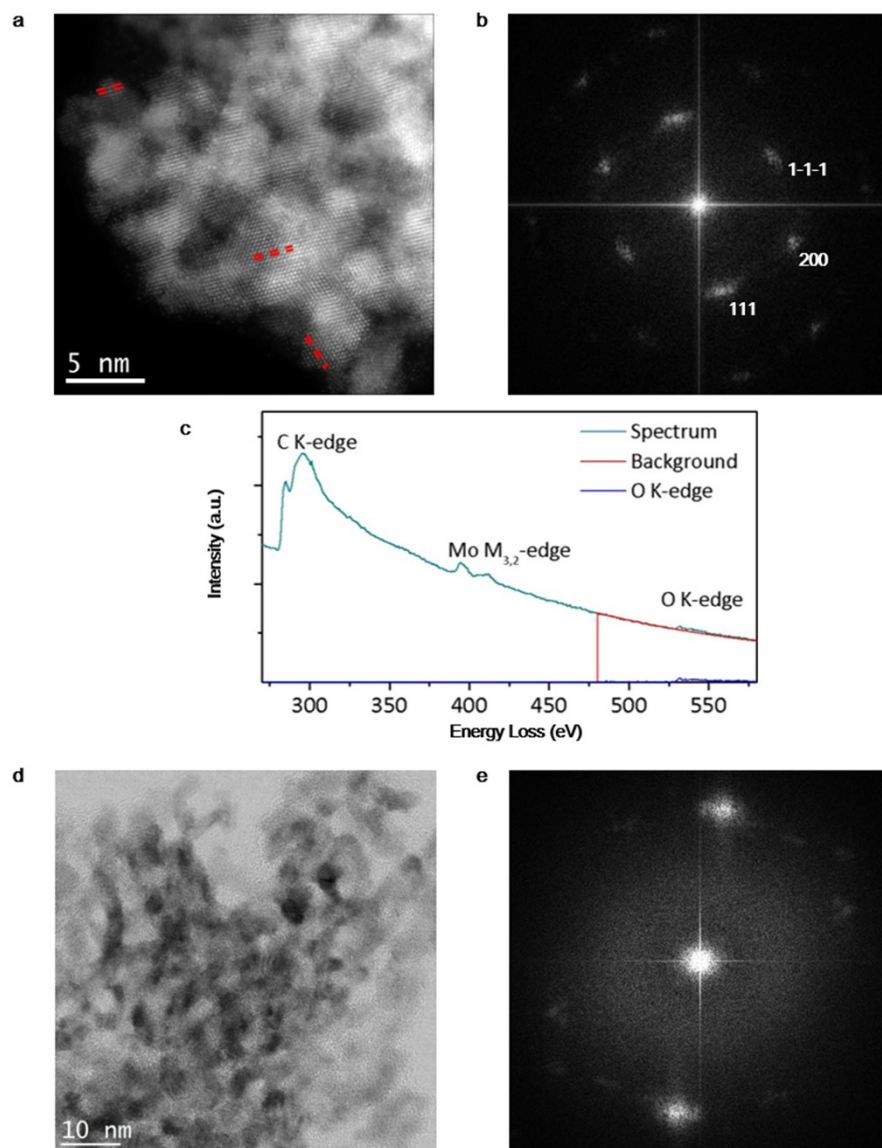
**Data availability.** The data that support the findings of this study are available from the corresponding authors on reasonable request.

29. Lee, J. S., Volpe, L., Ribeiro, F. H. & Boudart, M. Molybdenum carbide catalysts: II. Topotactic synthesis of unsupported powders. *J. Catal.* **112**, 44–53 (1988).
30. Ma, Y. et al. Low-temperature steam reforming of methanol to produce hydrogen over various metal-doped molybdenum carbide catalysts. *Int. J. Hydrogen Energy* **39**, 258–266 (2014).
31. Toby, B. H. EXPGUI, a graphical user interface for GSAS. *J. Appl. Cryst.* **34**, 210–213 (2001).
32. Ravel, B. & Newville, M. ATHENA, ARTEMIS, HEPHAESTUS: data analysis for X-ray absorption spectroscopy using IFEFFIT. *J. Synchrotron Radiat.* **12**, 537–541 (2005).
33. Krivanek, O. L. et al. in *Low Voltage Electron Microscopy: Principles and Applications* (eds Bell, D. & Erdman N.) 119–161 (Wiley-Blackwell, 2013).
34. Kresse, G. & Furthmüller, J. Efficiency of ab-initio total energy calculations for metals and semiconductors using a plane-wave basis set. *Comput. Mater. Sci.* **6**, 15–50 (1996).
35. Kresse, G. & Furthmüller, J. Efficient iterative schemes for ab initio total-energy calculations using a plane-wave basis set. *Phys. Rev. B* **54**, 11169–11186 (1996).
36. Blöchl, P. E. Projector augmented-wave method. *Phys. Rev. B* **50**, 17953–17979 (1994).
37. Kresse, G. & Joubert, D. From ultrasoft pseudopotentials to the projector augmented-wave method. *Phys. Rev. B* **59**, 1758–1775 (1999).
38. Perdew, J. P., Burke, K. & Ernzerhof, M. Generalized gradient approximation made simple. *Phys. Rev. Lett.* **77**, 3865–3868 (1996).
39. Henkelman, G., Uberuaga, B. P. & Jónsson, H. A climbing image nudged elastic band method for finding saddle points and minimum energy paths. *J. Chem. Phys.* **113**, 9901–9904 (2000).



**Extended Data Figure 1 | Structural characterization of Pt/MoC-based catalysts.** **a**, Rietveld structure refinement results obtained from XRD analysis of different Pt/MoC-based catalysts, including  $\alpha$ -MoC lattice constants and molar percentages of fcc  $\alpha$ -MoC. **b**, Molybdenum K-edge (20,000 eV) X-ray absorption near-edge structure (XANES) spectra of different Pt/MoC-based catalysts and of molybdenum foil and molybdenum oxides; the results suggest that no molybdenum oxide is present in the catalysts. **c–g**, Platinum L<sub>3</sub>-edge EXAFS fitting results for: **c**, 2%Pt/ $\alpha$ -MoC; **d**, 2%Pt/MoC-2; **e**, 2%Pt/MoC-3; **f**, 2%Pt/ $\beta$ -Mo<sub>2</sub>C; and **g**, 2% Pt/Al<sub>2</sub>O<sub>3</sub> catalysts in  $R$  space, where  $R$  represents the distance

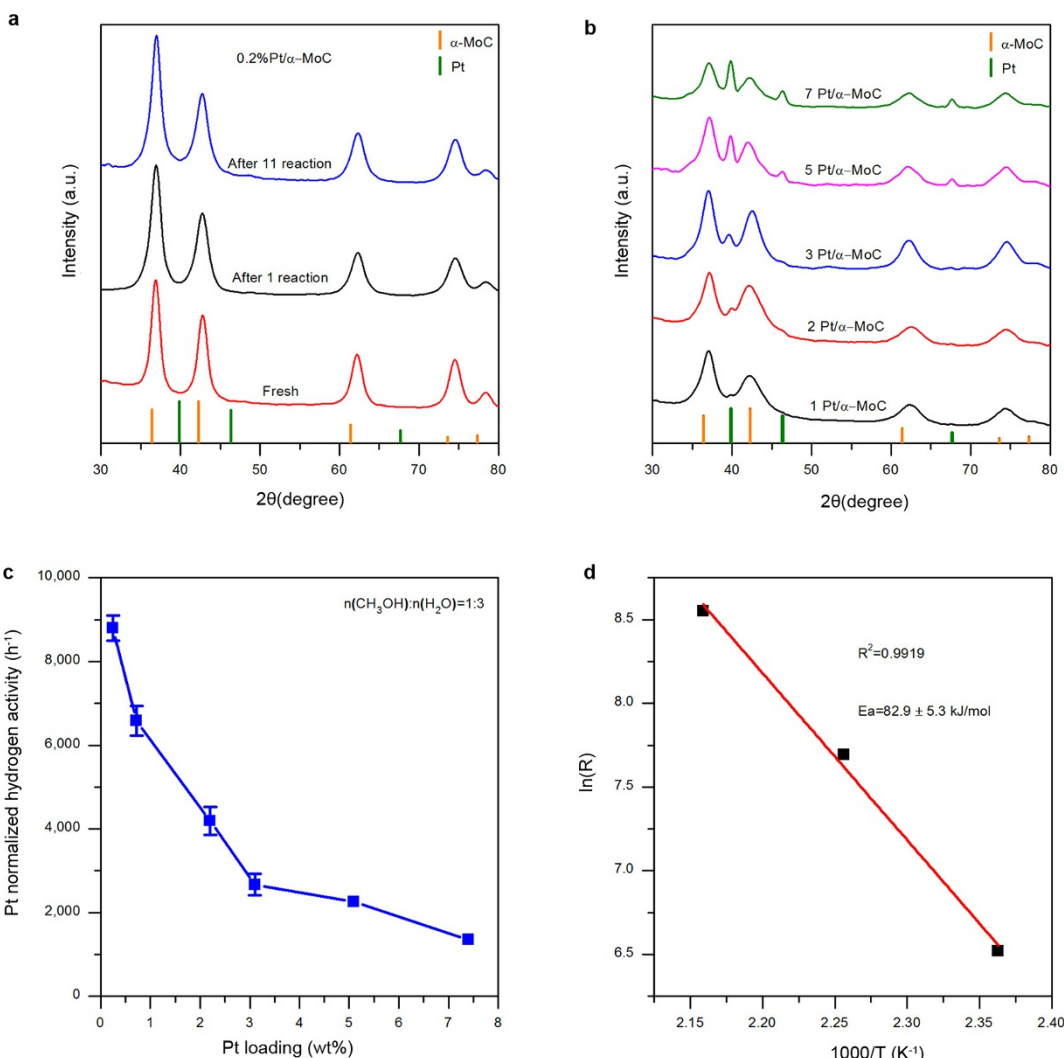
between scattering neighbour atoms and the absorbing atom, without correcting for scattering phase shift. The circles show the original data, and the red curve is the fitting curve; the areas enclosed by dotted green lines represent the fitting region. **h**, Corresponding platinum L<sub>3</sub>-edge XANES spectra for the catalysts, platinum foil and platinum oxides. The platinum L<sub>3</sub> ‘white line’ (the first maximum of the XANES curve after the absorption edge; dotted line) of Pt/ $\alpha$ -MoC catalysts moves to a higher energy than in metallic platinum foil, suggesting that platinum in the catalyst exhibits a positive charge.



**Extended Data Figure 2 | Electron microscopy characterization.**

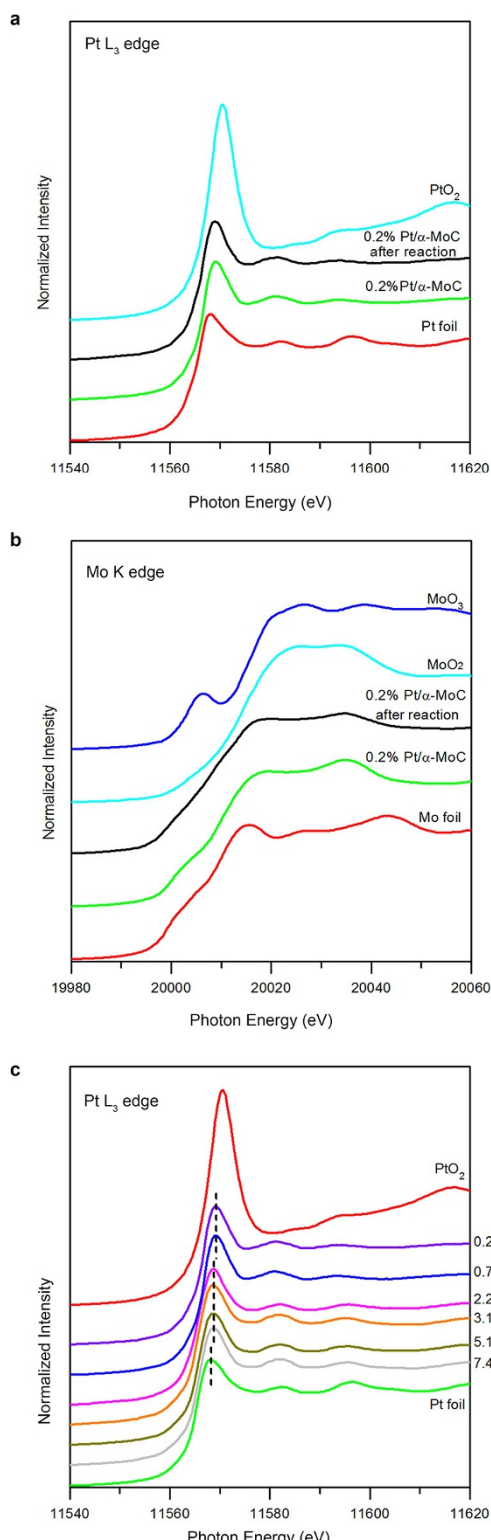
a, Low-magnification STEM Z-contrast image of 2% Pt/ $\alpha$ -MoC. b, Corresponding fast Fourier transform (FFT) pattern of the image, showing that the  $\alpha$ -MoC substrate has a fcc structure and is imaged along the  $[01\bar{1}]$  zone axis. The red dashed lines illustrate the  $\{111\}$  planes. The polycrystalline substrate is highly textured. c, Electron energy-loss spectrum (EELS) acquired from a  $16 \times 16 \text{ nm}^2$  region of the  $\alpha$ -MoC

substrate, showing the presence of a very small amount of oxygen and the strong molybdenum and carbon signals. d, STEM bright-field image of 0.2%Pt/ $\alpha$ -MoC catalyst. e, Corresponding FFT pattern. The  $\alpha$ -MoC support has a porous appearance, with highly textured nanocrystals of 2–6 nm in size. This textured structure shows a strong tendency to align along the  $\{111\}$  direction (as shown in the FFT pattern)—that is, the nanocrystals have strong tendency to expose the  $\{111\}$  surfaces.

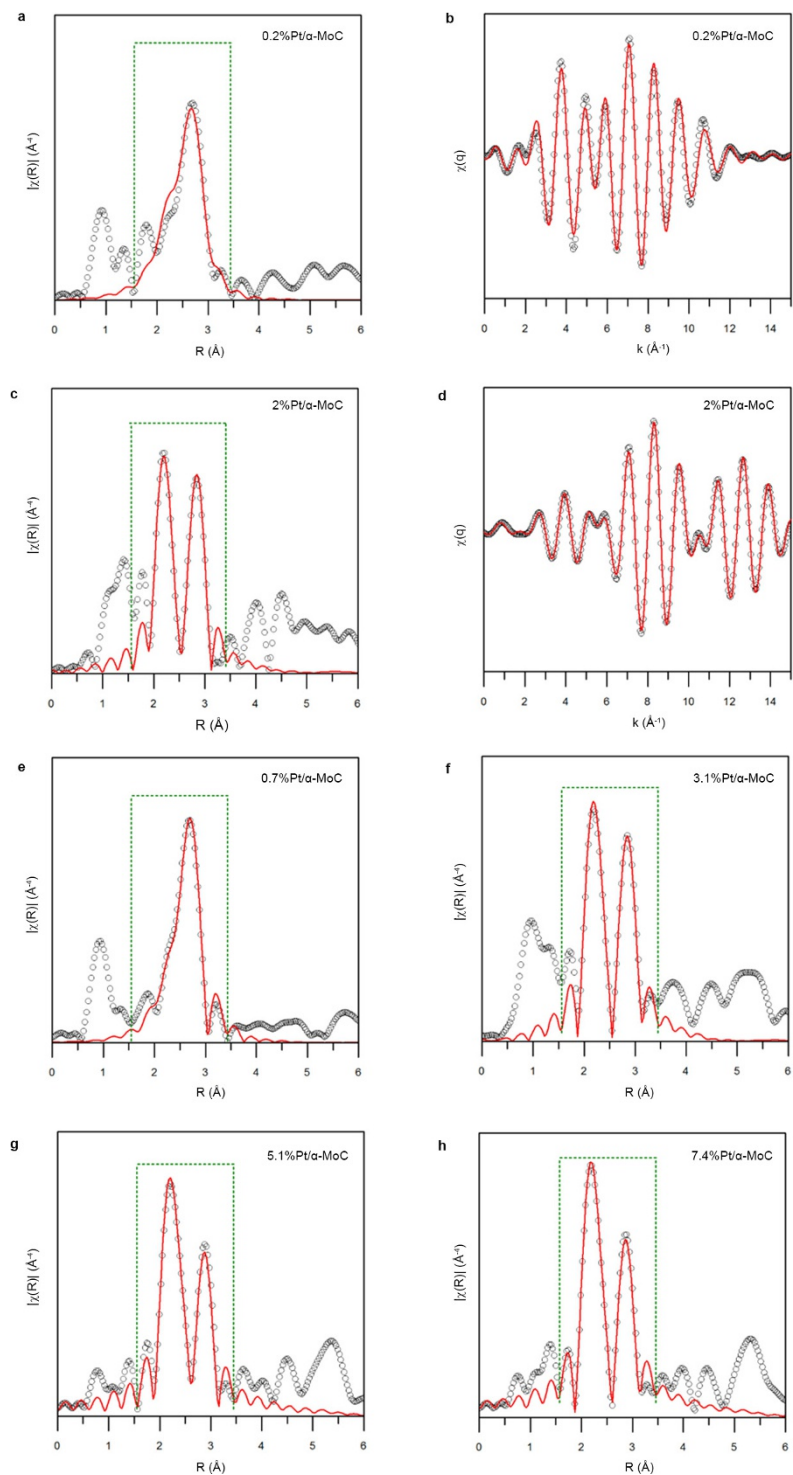


**Extended Data Figure 3 | XRD characterization and reaction kinetics.** **a**, XRD profiles of fresh and spent 0.2%Pt/α-MoC catalysts after 1 and 11 reaction cycles. The similar diffraction patterns suggest that this catalyst is stable under APRM conditions. There is no sign of bulk phase oxidation or phase transformation. The diffraction peaks of the α-MoC substrate appear at higher 2θ angles than the theoretical predicted values, indicating that the lattice constant of this substrate is slightly smaller than that of stoichiometric α-MoC. We ascribe the shift in the diffraction peaks to a deficiency in carbon as compared with the stoichiometric value. **b**, XRD profiles of Pt/α-MoC catalysts with different Pt loadings (0.7 wt%, 2.2 wt%, 3.1 wt%, 5.1 wt% or 7.4 wt%, numbered 1, 2, 3, 5 and 7, respectively, in the figure). XRD profiles were collected on a Rigaku X-ray diffractometer operated at 40 kV and 100 mA, using Cu K $\alpha$  radiation. We observed no peaks associated with Pt nanoparticles for

catalysts with Pt loading lower than 0.7%. However, when the Pt loading increases from 2.2 wt% to 7 wt%, a small peak associated with fcc Pt diffraction appears and increases gradually, indicating the presence and growth of Pt nanoparticles. **c**, Variation in catalytic activity (hydrogen evolution rate) versus Pt loading on Pt/α-MoC catalysts (190 °C;  $n(\text{CH}_3\text{OH}):n(\text{H}_2\text{O}) = 1:3$ ). The activity of catalysts with less than 3.1% Pt loading was determined in three parallel reactions. The activity values are the numerical averages; the error bars represent the standard deviation of the three tests. **d**, Arrhenius plot of the methanol-reforming reaction for 2%Pt/α-MoC. The estimated apparent activation energy ( $E_a$ ) is 82.9 kJ mol<sup>-1</sup>, similar to the reaction barrier energy calculated from DFT.  $R^2 = 0.9919$  is the coefficient of determination of the linear regression fitting.

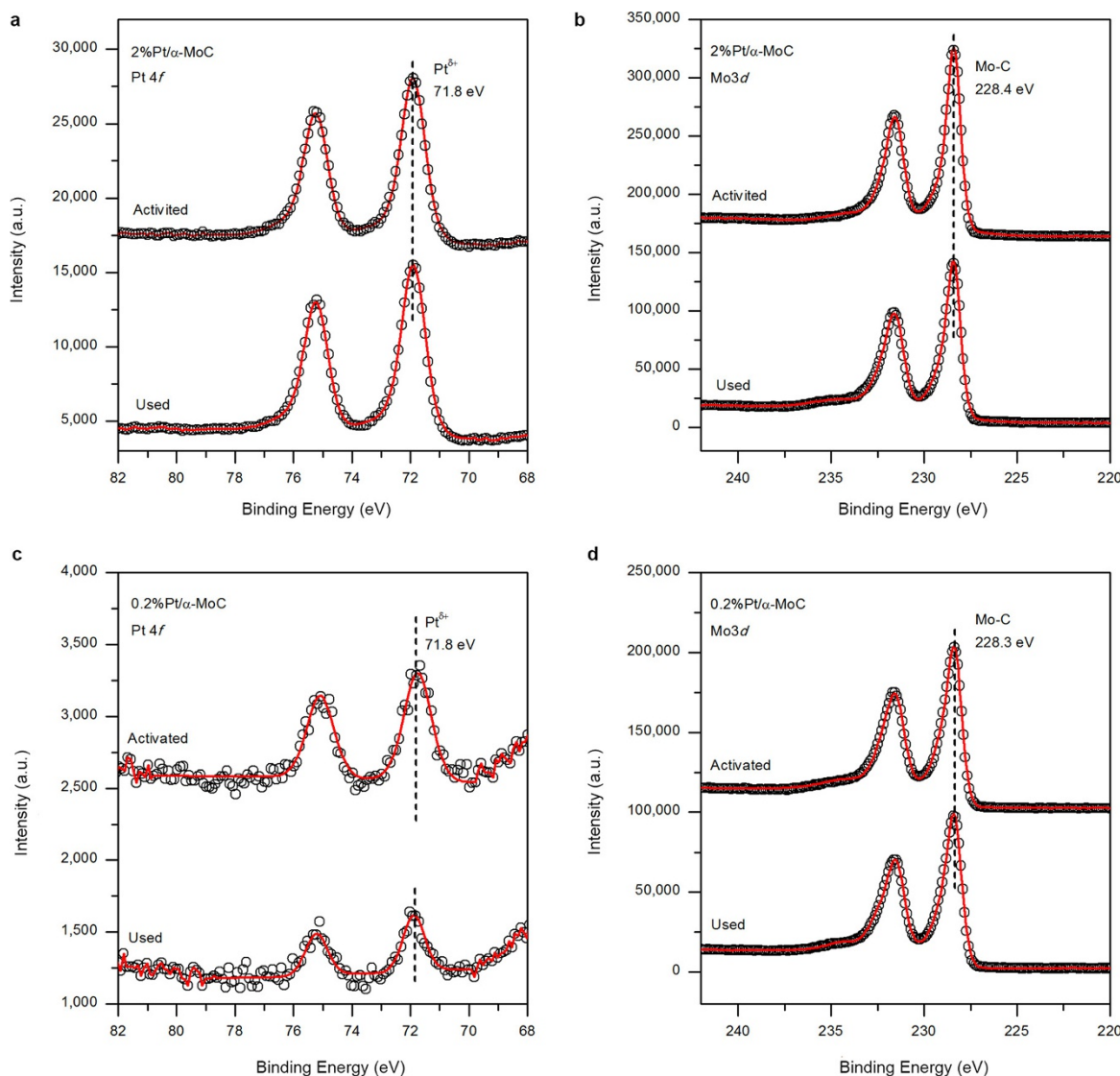

**Extended Data Figure 4 | XANES characterization of Pt/α-MoC.**

**a**, Platinum L<sub>3</sub>-edge and **b**, molybdenum K-edge XANES results from fresh and used 0.2%Pt/α-MoC. These XANES spectra suggest that charge transfer from platinum to molybdenum is unchanged after the reaction, and that there is no sign of bulk phase oxidation in α-MoC. **c**, Pt L<sub>3</sub>-edge XANES spectra of Pt/α-MoC catalysts with different Pt loadings. Platinum foil and platinum oxide were used as standards. The position of the ‘white line’ (dashed line) shows gradual positive movement (from 0.5 eV to 0.6 eV) with decreasing Pt loading.



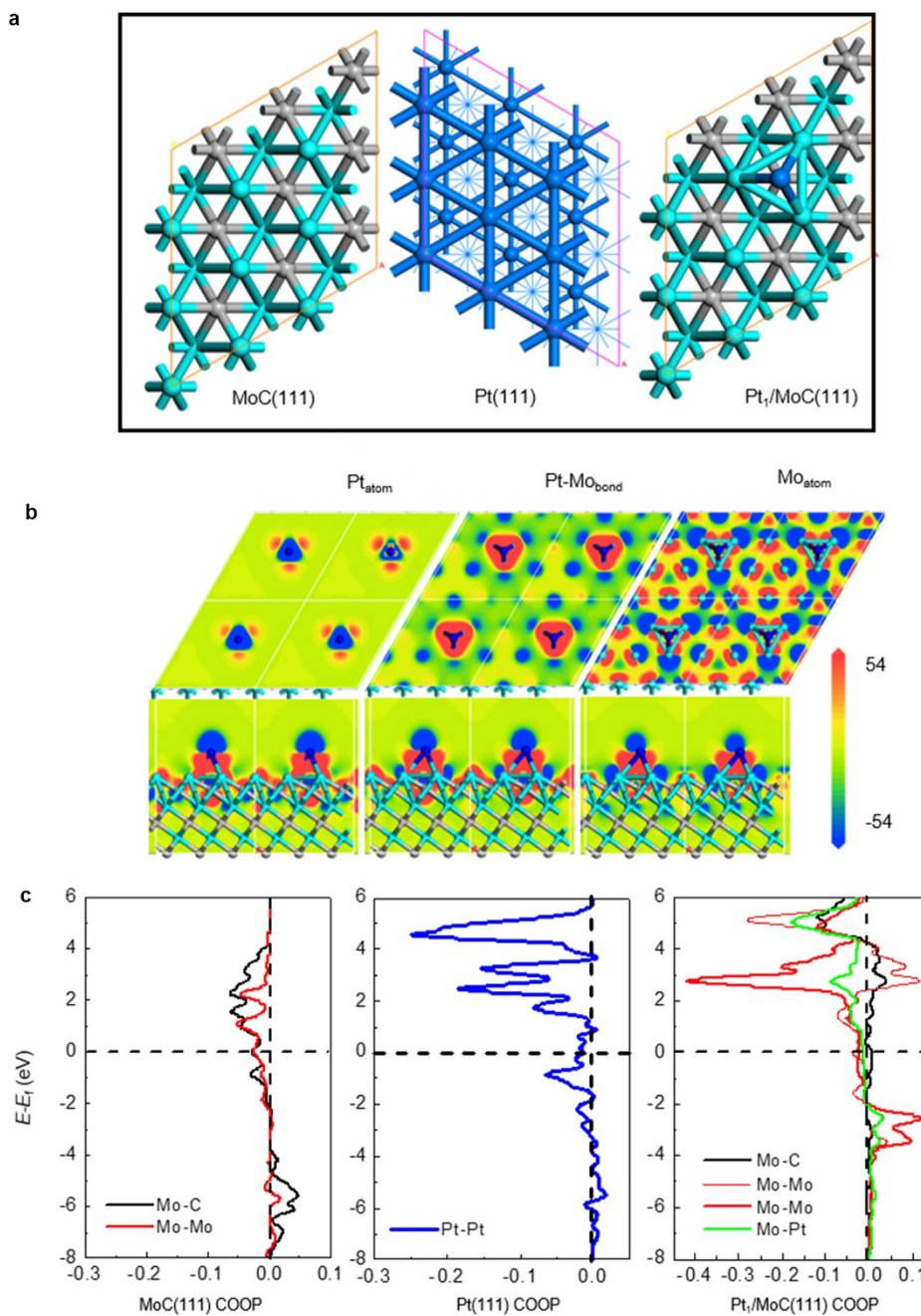
**Extended Data Figure 5 | Pt L<sub>3</sub>-edge EXAFS fitting results for Pt/α-MoC catalysts with different Pt loadings.** **a–d**, Fitting details for Pt L<sub>3</sub>-edge EXAFS spectra obtained for the 0.2%Pt/α-MoC catalyst (**a, b**) and the 2%Pt/α-MoC catalyst (**c, d**) as examples ('k' and 'q' refer to the

EXAFS annotation for the wavenumber of the photoelectron) **e–h**, Pt L<sub>3</sub>-edge EXAFS fitting results for **e**, 0.7%, **f**, 3.1%, **g**, 5.1%, and **h**, 7.4% Pt/α-MoC catalysts in R space (*k* weight = 3).



**Extended Data Figure 6 | XPS characterization of 2%Pt/α-MoC and 0.2%Pt/α-MoC.** **a**, XPS spectra of the platinum 4f regions (the binding energy of pure platinum foil is 71.2 eV) and **b**, the molybdenum 3d regions of 2%Pt/α-MoC before and after exposure to methanol/water vapour at 190 °C for 1 hour. Pt<sup>δ+</sup> denotes a partial positive charge on Pt. **c**, XPS spectra of the platinum 4f and **d**, molybdenum 3d regions of 0.2%Pt/α-MoC before and after exposure to methanol/water vapour at 190 °C for 1 hour. After the reaction, we detected no oxidation of platinum

in either catalyst (as compared with the fresh catalysts); however, we did observe oxidation of a small amount of molybdenum, as shown by the generation of weak components in the high-energy region. These findings show that: first, platinum is not oxidized during the reaction; and second, perhaps only the MoC domain that is far from the Pt<sub>1</sub> species is oxidized by the dissociated water, while oxygen-containing groups on the MoC domain adjacent to Pt<sub>1</sub> will be converted to CO<sub>2</sub> and H<sub>2</sub> through the ongoing reaction cycles.

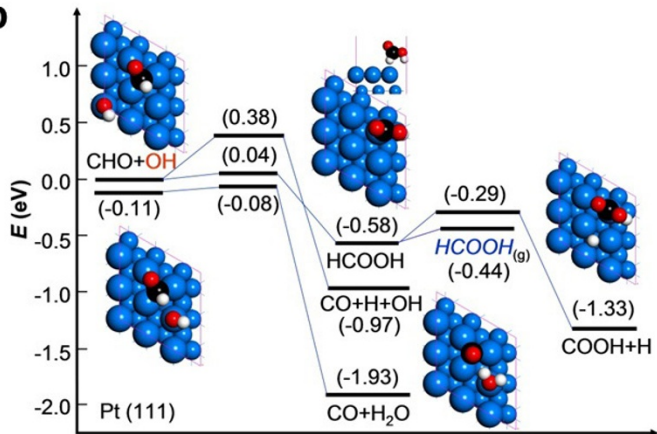
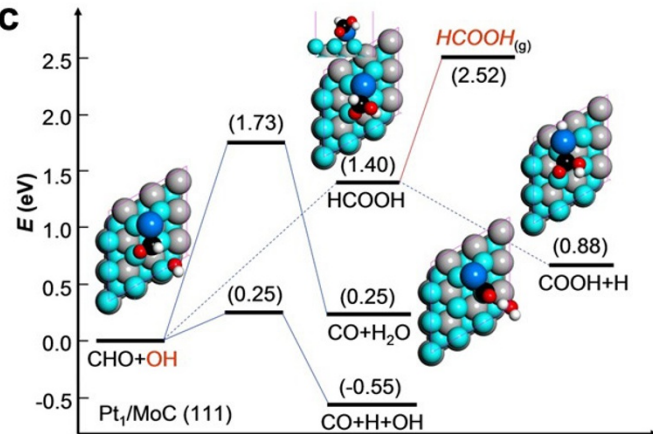
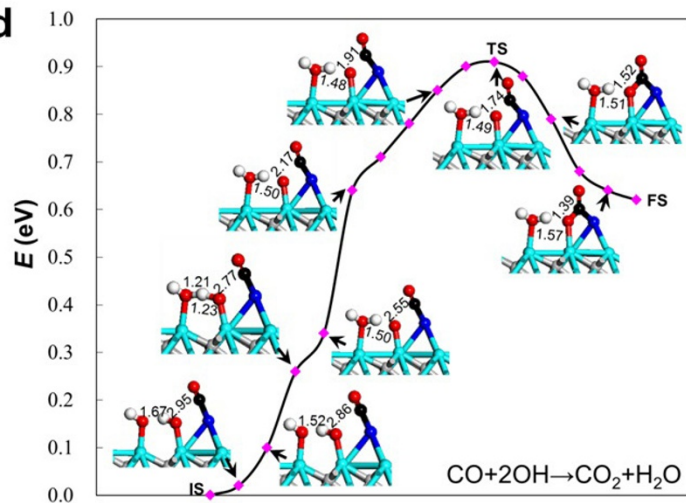


**Extended Data Figure 7 | Calculation models and electronic properties.** **a**, Top views of molybdenum-terminated  $\alpha$ -MoC(111) (representing the  $\alpha$ -MoC surface without loaded Pt), Pt(111) (representing pure Pt) and Pt<sub>1</sub>/ $\alpha$ -MoC structures obtained from DFT models. Blue, Pt atoms; cyan, Mo atoms; grey, C atoms. **b**, Charge-density differences for Pt atoms, Pt–Mo bonds and Mo atoms from Pt<sub>1</sub>/ $\alpha$ -MoC(111), in top and side views. Blue and red represent charge depletion and charge accumulation, respectively. Electron densities over the Pt and Mo sites in the catalyst are reduced greatly compared with the density over metallic Pt, while the Pt–Mo bonds form electron-rich regions. The units for the colour scale bar are a.u.<sup>-3</sup>. **c**, Crystal orbital overlap population (COOP) analysis of

the Mo–C and Mo–Mo bonds in  $\alpha$ -MoC(111), the Pt–Pt bond in Pt(111), and the Mo–C, Mo–Mo and Mo–Pt bonds in Pt<sub>1</sub>/ $\alpha$ -MoC(111). In a COOP analysis, all energies are measured with respect to the Fermi level; a bonding contribution is represented by a positive COOP and an anti-bonding contribution by a negative COOP. For example, it can be found that charge transfer from Pt to the Pt–Mo interface in the Pt<sub>1</sub>/ $\alpha$ -MoC(111) model effectively arouses the anti-oxidation ability of  $\alpha$ -MoC (as seen by looking at the Mo–C bonds: anti-bonding characters (a negative sign around the Fermi level) in MoC(111) become bonding characters (a positive sign) in Pt<sub>1</sub>/MoC(111), indicating a stronger Mo–C bond, which is related to anti-oxidation ability).

**a**

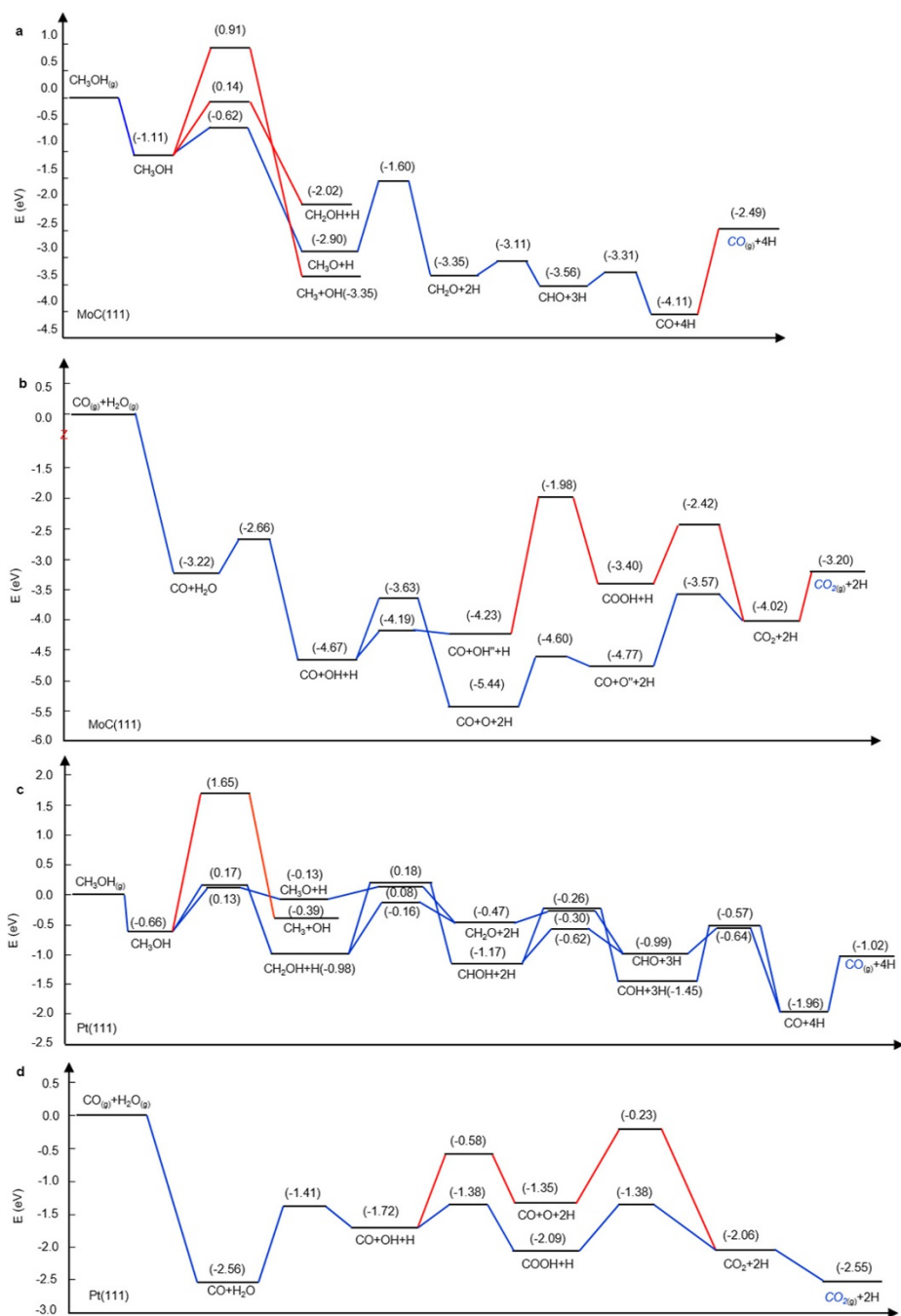
$E_{\text{ads}}$ (eV)	CH <sub>3</sub> OH	H <sub>2</sub> O	CO	CO <sub>2</sub>	2H	H <sub>2</sub>
$\alpha\text{-MoC}(111)$	-1.11	-0.94	-2.28	-1.44	-1.86	-0.83
Pt(111)	-0.66	-0.47	-2.59	-0.27	-1.06	/
Pt <sub>1</sub> / $\alpha\text{-MoC}(111)$	-1.30	-1.12	-2.04	-1.05	-1.68	-0.91

**b****c****d**

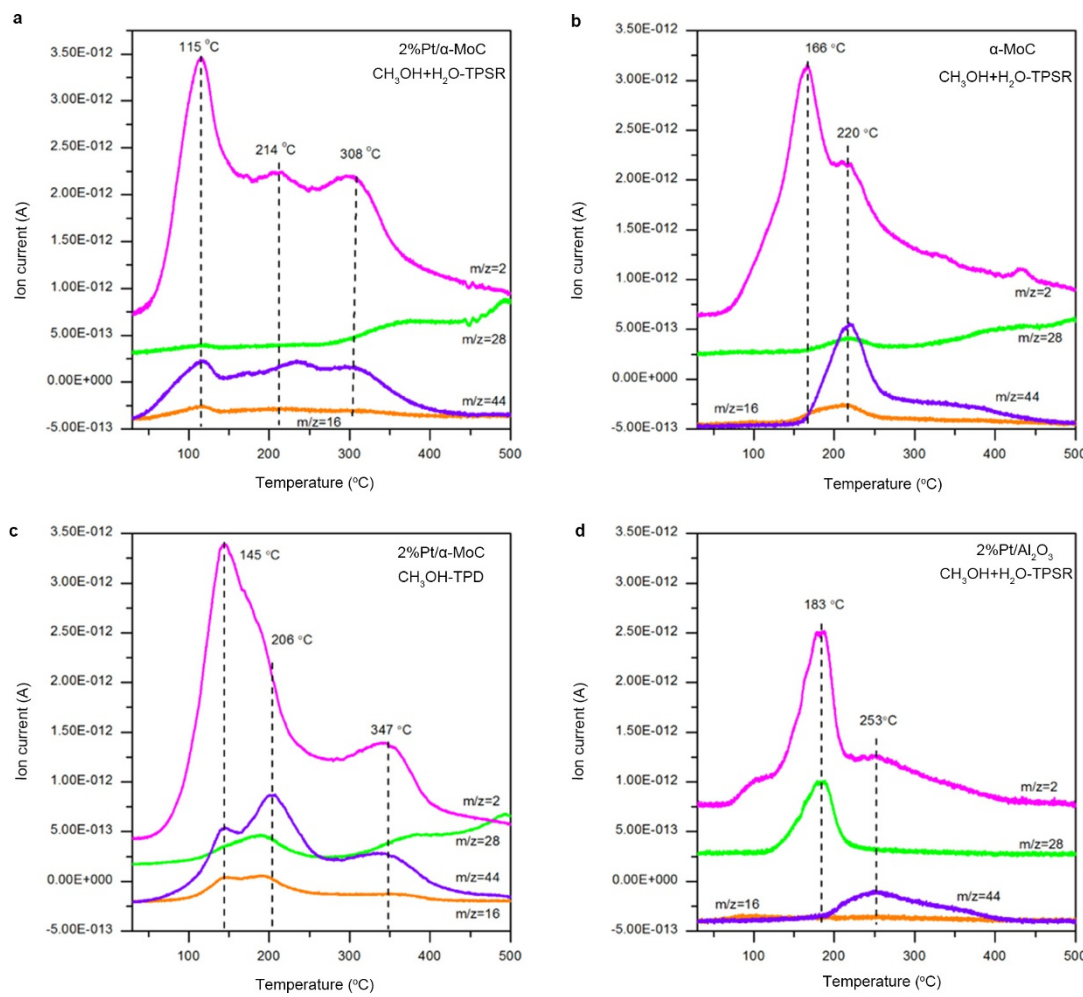
**Extended Data Figure 8 | Adsorption energies in surface models and some detailed reaction paths.** a, Adsorption energies ( $E_{\text{ads}}$ , measured in eV) of CH<sub>3</sub>OH, H<sub>2</sub>O, CO, CO<sub>2</sub>, H and H<sub>2</sub> in different surface models. b, c, Reaction pathways for the APRM-driven formation of formic acid (HCOOH) via OH oxidation on b, Pt(111) and c, Pt<sub>1</sub>/ $\alpha\text{-MoC}(111)$ . The energy profile for the HCOOH conversion route of methanol reforming

over the two models incorporates the zero-point energy and entropy correction at 463 K. The results suggest that the HCOOH route is not kinetically favoured as compared with the CHO dissociation route.

d, Intermediate structures and corresponding energies for elementary steps of the reaction  $\text{CO} + 2\text{OH} \rightarrow \text{CO}_2 + \text{H}_2\text{O}$ . TS, transition state; FS, final state.



**Extended Data Figure 9 | Energy profiles for methanol dissociation and the water–gas shift reaction on  $\alpha\text{-MoC}(111)$  and  $\text{Pt}(111)$ .** **a,** Methanol dissociation into CO and H atoms on  $\alpha\text{-MoC}(111)$ . **b,** Water–gas shift reaction on  $\alpha\text{-MoC}(111)$ . **c,** Methanol dissociation on  $\text{Pt}(111)$ . **d,** Water–gas shift reactions on  $\text{Pt}(111)$ .



**Extended Data Figure 10 | Studies of temperature desorption and surface reactions.** **a**, Temperature-programmed surface reaction (TPSR) of methanol and water over 2%Pt/α-MoC. The very-low-temperature H<sub>2</sub> generation with CO<sub>2</sub> at 115 °C is due to the methanol reforming with water. The signals around 214 °C are attributed to the reaction of methanol and water adsorbed at bare α-MoC sites. **b**, TPSR of methanol and water over α-MoC. At low temperatures (166 °C), no C-containing species is generated, indicating that α-MoC cannot dissociate the C–H bond of methanol at this temperature, let alone catalyse the successive reforming or decomposition processes. In other words, Pt<sub>1</sub> is indispensable for low-temperature C–H cleavage. Only at temperatures greater than 220 °C could α-MoC catalyse the methanol-reforming reaction. **c**, Temperature-programmed desorption (TPD) of methanol over 2%Pt/α-MoC. The

signals at 145 °C are attributed to the intermolecular reforming of methanol, and the signals at 206 °C signals come from the decomposition of methanol into CO, CO<sub>2</sub> and H<sub>2</sub>. **d**, TPSR of methanol and water over 2%Pt/Al<sub>2</sub>O<sub>3</sub>. Without α-MoC, Pt particles mainly catalyse methanol decomposition to CO and H<sub>2</sub>, as the signals at 183 °C show. Owing to the lack of surface hydroxyl from water dissociation at this temperature, CO<sub>2</sub> does not form, and can be detected only at higher temperatures. The results show that the α-MoC support in the 2%Pt/α-MoC catalyst serves as the centre of water dissociation and suppresses the side reaction of methanol decomposition at low temperatures. The combination of Pt<sub>1</sub> and α-MoC renders this catalyst capable of water dissociation, C–H bond activation and reformation, and thus a good choice for low-temperature hydrogen production.

**Extended Data Table 1 | Pt L<sub>3</sub>-edge EXAFS fitting results for Pt/MoC catalysts and the reference compound 2%Pt/Al<sub>2</sub>O<sub>3</sub>**

Catalysts	Shell	Bond length (Å)	C.N. *	$E_0$ shift (eV) †	$\sigma^2$ (Å <sup>2</sup> ) ‡
<b>Pt/MoC catalysts and reference</b>					
2%Pt/ $\alpha$ -MoC	Pt-Pt	2.78+/-0.01	4.8+/-0.7	6.4	0.005
	Pt-Mo	2.78+/-0.01	3.2+/-0.7		0.006
2%Pt/MoC-2	Pt-Pt	2.76+/-0.01	5.2+/-0.9	5.6	0.005
	Pt-Mo	2.76+/-0.01	2.6+/-0.7		0.004
2%Pt/MoC-3	Pt-Pt	2.76+/-0.01	6.2+/-0.8	5.6	0.004
	Pt-Mo	2.76+/-0.01	2.2+/-0.5		0.004
2%Pt/ $\beta$ -Mo <sub>2</sub> C	Pt-Pt	2.76+/-0.01	6.5+/-0.9	5.3	0.005
	Pt-Mo	2.75+/-0.01	1.6+/-0.5		0.003
2%Pt/Al <sub>2</sub> O <sub>3</sub>	Pt-Pt	2.76+/-0.01	7.2+/-1.6	7.5	0.007
	Pt-O	2.02+/-0.03	1.7+/-0.7		0.009
<b>Catalysts with different Pt loadings</b>					
0.2%Pt/ $\alpha$ -MoC	Pt-Pt	--	--	5.9	--
	Pt-Mo	2.85+/-0.01	6.8+/-1.0		0.015
0.7%Pt/ $\alpha$ -MoC	Pt-Pt	3.01+/-0.01	1.9+/-1.3	7.5	0.009
	Pt-Mo	2.88+/-0.01	6.0+/-1.3		0.012
2.2%Pt/ $\alpha$ -MoC	Pt-Pt	2.78+/-0.01	4.8+/-0.7	6.4	0.005
	Pt-Mo	2.78+/-0.01	3.2+/-0.7		0.006
3.1%Pt/ $\alpha$ -MoC	Pt-Pt	2.76+/-0.01	4.4+/-1.0	6.7	0.004
	Pt-Mo	2.76+/-0.01	3.3+/-0.8		0.005
5.1%Pt/ $\alpha$ -MoC	Pt-Pt	2.76+/-0.01	4.3+/-1.0	6.3	0.005
	Pt-Mo	2.76+/-0.01	3.0+/-0.7		0.005
7.4%Pt/ $\alpha$ -MoC	Pt-Pt	2.75+/-0.01	5.2+/-1.0	5.9	0.005
	Pt-Mo	2.75+/-0.01	2.7+/-0.7		0.003
<b>0.2% Pt/<math>\alpha</math>-MoC catalysts before and after reaction</b>					
Fresh	Pt-Pt	--	--	5.9	--
	Pt-Mo	2.85+/-0.01	6.8+/-1.0		0.015
Used	Pt-Pt	--	--	5.9	--
	Pt-Mo	2.84+/-0.01	6.4+/-1.1		0.013

\*C.N., coordination number.

†The difference in inner potential (the zero-point energy of photoelectrons) between the measured sample and standards.

‡Mean-square relative displacement, which measures the disorder of neighbouring atoms.